ROYAL SOCIETY
OF CHEMISTRY

PAPER

Check for updates

Glassy and liquid Sb₂S₃: insight into the structure and dynamics of a promising functional material†

Mohammad Kassem,[a] Chris J. Benmore,[b] Andrey Tverjanovich, [c] Takeshi Usuki,[d] Maxim Khomenko,[e] Daniele Fontanari,[a] Anton Sokolov, [a] Koji Ohara, [f] Maria Bokova, [a] Shinji Kohara [g] and Eugene Bychkov *[a]

Antimony sesquisulfide Sb₂S₃ has become an outstanding advanced functional material in a variety of rapidly growing application fields: smart integrated photonics from the visible to telecom window, cost-efficient photovoltaics, energy storage and transformation. Rational design and tailoring of the required components need a deep insight into the atomic structure and dynamics of liquid and amorphous Sb₂S₃, but detailed information is missing in contrast to crystalline counterparts. Using high-energy X-ray diffraction and Raman spectroscopy over an extended temperature range, supported by first-principles simulations as well as by electrical and thermal studies, we show that the high optical and electric contrast between the SET (crystalline) and RESET (amorphous) logic states is related to the different short and intermediate range order in orthorhombic and vitreous Sb₂S₃. It includes strong asymmetry of the Sb–S nearest neighbor distances and a different coordination of antimony sites in the crystal *vs.* a distorted trigonal environment of defect octahedral SbS₃ entities in glassy Sb₂S₃. A fast crystallization rate at elevated temperatures in liquid antimony sesquisulfide is related to the enhanced fragility, approaching that of telluride phase-change materials, and to a large fraction of ABAB squares (A: Sb; B: S), combined with a remarkable slowdown of the diffusion processes in the vicinity of the glass transition temperature, ensuring good retention of the amorphous state. Further improvements may be achieved using anionic (Se) or cationic (Bi) substitution that decreases the temperature of a semiconductor–metal transition and allows bandgap engineering, important for both photonics and photovoltaics.

a Laboratoire de Physico-Chimie de l'Atmosphère, Université du Littoral Côte d'Opale, 59140 Dunkerque, France. E-mail: bychkov@univ-littoral.fr

b X-ray Science Division, Advanced Photon Source, Argonne National Laboratory, Argonne, Illinois 60439, USA

c Institute of Chemistry, St. Petersburg State University, 198504 St. Petersburg, Russia

d Faculty of Science, Yamagata University, Yamagata 990-8560, Japan

e ILIT RAS-Branch of the FSRC "Crystallography and Photonics" RAS, 140700 Shatura, Moscow Region, Russia

f Research and Utilization Division, Japan Synchrotron Radiation Research Institute, 1-1-1 Kouto, Sayo, Hyogo 679-5198, Japan

g Quantum Beam Field, Research Center for Advanced Measurement and Characterization, National Institute for Materials Science, 1-2-1 Sengen, Tsukuba, Ibaraki 305-0047, Japan

† Electronic supplementary information (ESI) available: Raw diffraction patterns of Sb₂S₃, Raman spectrum of amorphous antimony, evolution of Raman spectra for Sb₂S₃ as a function of temperature, DFT Raman spectra of size-limited clusters, S–Sb–S bond angle distributions for DFT-optimized clusters, distributions of Sb–S interatomic distances in DFT-optimized clusters, diffraction data for glassy and liquid As₂S₃, comparison of FPMD modeling with standard PBE and hybrid PBE0 functionals, FPMD modeling of glassy As₂S₃ under high-pressure, fitting Sb–S partials with asymmetric functions, coordination distributions of sulfur and antimony, bond angle distributions in glassy and liquid Sb₂S₃, FPMD partial pair-distribution functions in g-Sb₂S₃ and g-As₂S₃, derived Sb and S diffusion coefficients plotted on the Arrhenius scale, and FPMD estimation of the semiconductor–metal (SC–M) transition temperature $T_{SC–M}$ for liquid Sb₂S₃. See DOI: https://doi.org/10.1039/d3tc00081h

1. Introduction

Antimony sesquisulfide Sb₂S₃ appears to be an emerging and promising advanced functional material for a variety of rapidly growing application fields:

(1) Wide gap phase-change materials (PCM) for both electrically and light tunable visible photonics or ultralow loss photonics at telecommunication wavelengths. Sb₂S₃ can be used for smart reprogrammable photonic systems with a nanosecond switching time, holographic and nonvolatile ultrathin displays of extremely high resolution, integrated photonic circuits, switchable metasurfaces and varifocal metalenses, nanophotonic and on-chip devices, dielectric nanoantennas, *etc.*[1–6]

(2) High-performance composite anodes for sodium and lithium batteries. Antimony sesquisulfide nanorods, nanoparticles and powders, sometimes combined with other sulfides and encapsulated into a doped carbon matrix or activated carbon, provide superior rate capability, excellent cyclic stability and capacity retention, as well as fast-charging capacity and highly decreased interfacial resistance.[7–10]

(3) Alternative absorber materials for thin-film solar cells. Antimony sulfide thin films belong to emerging earth-abundant

4654 | *J. Mater. Chem. C*, 2023, **11**, 4654–4673

This journal is © The Royal Society of Chemistry 2023

low-cost photovoltaic materials having a reasonable optical band-gap, tremendous low-light harvesting, and excellent moisture and air stability.[11,12]

(4) Thermoelectric materials. The high thermoelectric power of Sb_2S_3 seems to be promising for thermoelectric applications.[13] However, nanostructured or amorphous antimony sesquisulfide is mostly used as a dopant decreasing the thermal conductivity and increasing the Seebeck coefficient of composite thermoelectrics (lead chalcogenides, $(Bi,Sb)_2Te_3$, *etc.*) yielding a significantly enhanced figure of merit zT.[14,15]

Rational design and tailoring of optimized functional materials based on Sb_2S_3 need a deep insight into the atomic structure and dynamics of antimony sesquisulfide. The crystal structure of Sb_2S_3 has been extensively studied both under ambient conditions[16–18] and under high pressure.[19–26] Nevertheless, the atomic structure of vitreous and liquid antimony sesquisulfide is largely unknown except for classical X-ray diffraction studies of glassy Sb_2S_3 reported forty years ago and suffering from a limited accessible Q-range and insufficient r-space resolution.[27–29] In the case of PCM applications,[30–32] special attention should be paid to the origin of a high optical and electric contrast between the SET (crystalline) and RESET (amorphous) logic states since antimony sesquisulfide differs considerably from the benchmark telluride PCM ($GeTe$-Sb_2Te_3, GST, or doped Sb_2Te) in both chemical bonding and local antimony environments. The metavalent bonding[33] seems to be missing in Sb_2S_3; and the four-fold coordinated antimony sites, present in GST and a-Sb_2Te_3,[34,35] were not observed in vitreous Sb_2S_3,[27–29] even though there is a controversy in amorphous tellurides related to the antimony local order.[36,37]

Using high-energy X-ray diffraction and Raman spectroscopy supported by first-principles simulations, we will unravel a detailed structural organization of bulk glassy and liquid Sb_2S_3 over an extended temperature range, $298 \leq T \leq 1143$ K. Thermal properties and electrical conductivity measurements will also be provided showing a remarkable contrast in electronic properties between amorphous, crystalline and liquid states. Finally, the diffusion coefficients and viscosity of liquid Sb_2S_3 will be computed and compared with known experimental data, which reveal a significant fragility of molten antimony sesquisulfide in comparison with canonical dielectric As_2S_3. All these results will explain the promising PCM performance of Sb_2S_3 and an overall trend in functional properties going down the periodic table.

2. Experimental and methods

2.1 Glassy and nanocrystalline Sb_2S_3 preparation

A two-step synthesis was applied for glassy Sb_2S_3. First, a crystalline sample was prepared from high-purity antimony (99.999%, Cerac) and sulfur (99.999%, Alfa Aesar) in an evacuated and sealed silica tube. Then, a small quantity of c-Sb_2S_3 was placed in a thin-walled silica capillary, evacuated to 10^{-4} mbar and sealed. The capillary was slowly heated in a furnace to 1050 K and kept at this temperature for one hour with

subsequent cooling to 900 K. After an additional equilibration step for at least 30 minutes, the sample was splat-quenched under an argon atmosphere onto a fused silica plate cooled down to ≈ 80 K. Nanocrystalline nc-Sb_2S_3 was obtained by fast cooling in a silica capillary but without splat-quenching, that is, the estimated cooling rate was $\lesssim 1000$ K s^{-1}.

2.2 Thermal and electrical measurements

A TA instruments Q200 thermal analyzer was used for differential scanning calorimetry (DSC). The synthesized samples of 3–5 mg were encapsulated in a sealed aluminum pan and heated at a rate of 10 K min^{-1} under a dry nitrogen atmosphere to determine the glass transition T_g and crystallization temperatures. The ac and dc conductivity measurements were done over the $330 \leq T \leq 450$ K temperature range. A Hewlett Packard 4339B high resistance meter with applied voltage of 100 volts was used for the dc experiments. The ac conductivity over the 100 Hz to 15 MHz frequency range was measured using a Hewlett Packard 4194A impedance meter.

2.3 Raman spectroscopy measurements

A LabRam HR microRaman spectrometer (Jobin Yvon Horiba Group) was used for the measurements at room temperature. Raman scattering was excited by a 785 nm solid-state laser and recorded in the 50–850 cm^{-1} spectral range. The laser power was 0.75 mW. Two to three spectra were registered for each sample at different positions to verify the sample homogeneity and the absence of photoinduced phenomena. Raman spectra over the temperature range $293 \leq T \leq 873$ K were measured using a Senterra Raman spectrometer (Bruker) equipped with a microscope and a Linkam TS1000 hot stage. The spectra were excited by a 785 nm laser diode with a power of 1 mW and recorded in the 75–1500 cm^{-1} spectral range (reliable data above 100 cm^{-1}). Glassy Sb_2S_3 was placed in a silica tube (2 mm ID/3 mm OD, length 25 mm) and sealed under vacuum.

2.4 High-energy X-ray diffraction

The 6-ID-D beamline at the Advanced Photon Source (Argonne National Laboratory, Chicago) was used for high-energy X-ray diffraction measurements under ambient conditions and as a function of temperature. The photon energy was 99.9593 keV, and the wavelength was 0.124035 Å. A two-dimensional (2D) setup was used for data collection with a Varex area detector, 2880 × 2880 pixels, and a pixel size of 150 × 150 μm^2. The sample-to-detector distance was 287.7 mm for a room-temperature setup, and 334.9 mm for furnace measurements over the $673 \leq T \leq 1143$ K temperature range on cooling. Cerium dioxide was used as a calibrant. The exposure time was 0.2 s × 1500 frames, using one dark-field image file followed by five light files. Glass samples were fixed on a Kapton tape for the room temperature measurements. A Sb_2S_3 sample in evacuated silica tube (2 mm ID/3 mm OD) was used for the furnace experiments. The 2D diffraction patterns were reduced using the Fit2D software.[38] The measured background intensity (either the Kapton tape or the empty silica at various temperatures) was subtracted, and corrections were made for the

This journal is © The Royal Society of Chemistry 2023

J. Mater. Chem. C, 2023, **11**, 4654–4673 | **4655**

different detector geometries and efficiencies, sample self-attenuation, and Compton scattering using standard procedures,[39] providing the X-ray structure factor $S_X(Q)$.

$$S_X(Q) = w_{SbSb}(Q)S_{SbSb}(Q) + w_{Sbs}(Q)S_{Sbs}(Q) + w_{SS}(Q)S_{SS}(Q), \quad (1)$$

where $w_{ij}(Q)$ are Q-dependent X-ray weighting coefficients and $S_{ij}(Q)$ the Faber–Ziman partial structure factors. Typical raw diffraction data for nanocrystalline and glassy Sb_2S_3 are shown in Fig. S1 (ESI†).

Canonical As_2S_3 glass and liquid were also additionally measured at the BL04B2 beamline of the SPring-8 facility (Hyogo Prefecture, Japan) using a dedicated two-axis diffracto-meter equipped with four CdTe detectors at low angles and three Ge diodes at high diffraction angles.[40] The temperature measurements were carried out from 300 to 1223 K in a furnace. The 7-detector setup and incident X-ray energy of 112.6386 keV allows the diffraction pattern to be collected up to $Q = 30$ Å^{-1} with a high signal-to-noise ratio and sufficient energy resolution to discriminate both fluorescence from the sample and higher harmonic reflections from the mono-chromator crystal. The empty silica tube at different temperatures was also measured and used for background intensity subtraction. Further data analysis included absorption, Compton scattering, and polarization corrections using standard procedures[41] giving the total X-ray structure factor of $S_X(Q)$.[42,43]

2.5 First-principles simulations

The DFT calculations of vibrational spectra were carried out using Gaussian 16 software.[44] The structural optimization and harmonic vibrational frequency calculations were performed for size-limited clusters: $SbSb_3H_3$, SbS_3H_3, $Sb_2S_4H_2$ (chair and boat conformations), $Sb_2S_5H_4$, $Sb_2S_6H_4$, $Sb_3S_6H_3$, $Sb_6S_{12}H_6$, $Sb_{12}S_{18}H_2$, and $Sb_{12}S_{16}$. The Becke three-parameter hybrid exchange functional[45] and the Lee–Yang–Parr correlation functional (B3LYP)[46] were used for these simulations. The small-core relativistic pseudopotential basis set (cc-pVTZ-PP)[47] and the effective core potentials[48] were applied for cluster geometry optimization and Raman intensity calculations. Most of the structures were optimized using the tight convergence option ensuring adequate convergence and reliability of computed wavenumbers. An extra quadratically convergent self-consistent field procedure[49] was used for difficult convergence cases. Further details of the DFT simulations are reported elsewhere.[50–52]

Modeling of the diffraction data was carried out using Born–Oppenheimer molecular dynamics implemented within the CP2K package.[53] The generalized gradient approximation (GGA) and the PBE0 hybrid[54,55] exchange–correlation functional combining the exact Hartree–Fock and DFT approaches were used, providing better agreement with experiment.[56–59] The Grimme dispersion corrections D3BJ[60] were also employed, improving first-principles molecular dynamics (FPMD) results for chalcogenide systems.[61,62] The applied FPMD technique was similar to previous reports.[34,63] The initial atomic configurations for vitreous Sb_2S_3 were created and optimized using the RMC_POT++ code[64] against the experimental $S_X(Q)$. The size of the cubic simulation box, containing 200 atoms

(80 Sb and 120 S), was chosen to match the experimental density. Further optimization was carried out using DFT, applying the molecularly optimized correlation consistent polarized triple-zeta valence basis set along with the norm-conserving relativistic Goedecker–Teter–Hutter-type pseudo-potentials.[65] FPMD simulations were performed using a canonical NVT ensemble with a Nosé–Hoover[66,67] thermostat. The simulation boxes were heated from 300 K to 900 K using 100 K steps for 20–25 ps each. At 900 K (above melting), the systems were equilibrated for 70 ps and cooled down to 300 K using the same temperature steps but with a longer simulation time (25–45 ps). Final equilibration and data collection at 300 K were performed for 59 ps. Additional simulations were carried out between 850 and 1150 K (step 100 K for 40–50 ps each) consistent with the experimental data. The connectivity and ring statistics were analyzed using the R. I. N. G. S. package[68] and a modified connectivity program.[69] The pyMolDyn code[70] applying the Dirichlet–Voronoi tessellation was used for the calculation of microscopic voids and cavities.

3. Results and discussion

3.1 Glass-forming, thermal and electric properties

Glassy antimony sesquisulfide was reported to be a difficult material to vitrify.[27] Nevertheless, the applied splat-quenching technique[56] in thin-walled silica capillaries allows fully vitreous small droplets of g-Sb_2S_3 to be obtained. Typical DSC traces for glassy Sb_2S_3 and canonical g-As_2S_3 are shown in Fig. 1. The two end-members are consistent with the reported thermal properties for $(Sb_2S_3)_x(As_2S_3)_{1-x}$ pseudo-binaries, $x \leq 0.9$:[71–73] the glass transition temperature T_g monotonically increases with x from 472 K ($x = 0$) to 492 K ($x = 1$), the exothermic crystallization feature emerges above $x = 0.5$, grows and shifts toward lower T, emphasizing the increasing crystallization ability.

The conductivity temperature dependences $\sigma(T)$ for glassy and crystalline (this work), and molten[74] Sb_2S_3 are shown in Fig. 2 using an Arrhenius plot:

$$\sigma(T) = \sigma_0 \exp(-E_a/k_B T), \quad (2)$$

where σ_0 is the pre-exponential factor, E_a is the conductivity activation energy, and k_B and T have their usual meaning. We note a significant electrical contrast between glassy and crystalline samples, ≈ 4.5 orders of magnitude at room temperature with the corresponding difference in activation energy, $E_a^{cryst} = 0.733$ eV but $E_a^{glass} = 1.009$ eV. The conductivity increases on melting by three orders of magnitude compared to the extrapolated glass value, while the activation energy drops nearly by a factor of 2. The pre-exponential factor appears to be very similar for all three Sb_2S_3 phases, $400 \leq \sigma_0 \leq 800$ S cm^{-1}, and indicates a conductivity mechanism over extended (delo-calized) electron states.[75] The obtained results are consistent with the reported values of conductivity parameters and optical bandgap E_g for bulk crystalline samples and amorphous or crystalline thin films, $1.5 \leq E_g$ (c-Sb_2S_3) ≤ 1.8 eV and $2.0 \leq E_g$

4656 | *J. Mater. Chem. C*, 2023, **11**, 4654–4673

This journal is © The Royal Society of Chemistry 2023
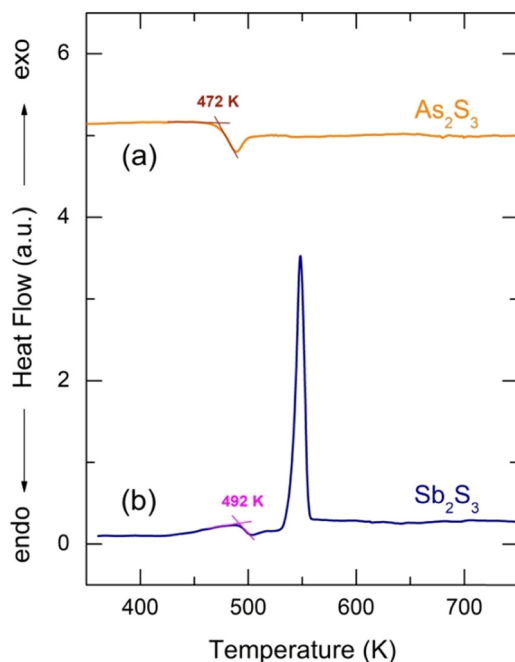
Fig. 1 DSC traces of glassy (a) As_2S_3 and (b) Sb_2S_3. The derived glass transition temperatures are also indicated.
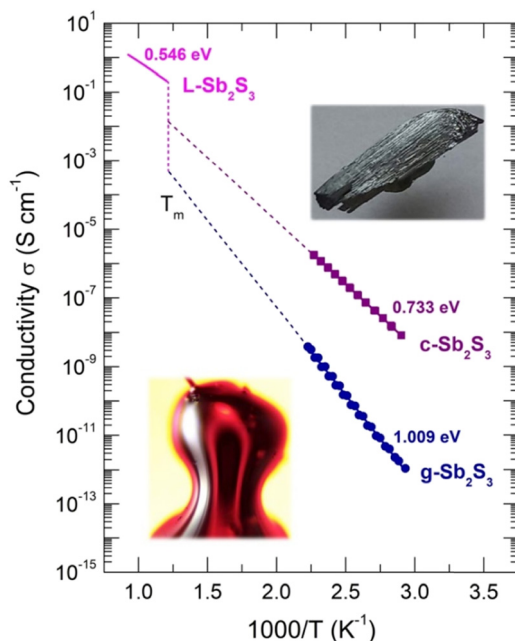

Fig. 2 Conductivity $\sigma(T)$ of glassy (g), crystalline (c) samples (this work), and liquid L-Sb_2S_3.[74] The inserts show g-Sb_2S_3 and c-Sb_2S_3.

(a-Sb_2S_3) $\leq$ 2.4 eV.[1,76–79] In addition, the conductivity seems to be intrinsic since $2E_a \cong E_g$.

3.2 Nanocrystalline Sb_2S_3

An insufficiently rapid quenching rate or wrong starting temperature for splat-cooling yields a nanocrystalline alloy, which

is slightly different from the stable orthorhombic polymorph, space group *Pnma*.[16] The observed Bragg peaks mostly correspond to orthorhombic antimony sesquisulfide, but we should note slight deviations of the peak positions and their different amplitudes compared to the reference compound (Fig. 3(a)). Besides, a non-negligible amorphous fraction is also present and possibly some traces of monoclinic high-T Sb_2S_3 polymorph, which is metastable at room temperature.[18]

The X-ray total correlation function $T_X(r)$ of nanocrystalline Sb_2S_3, Fig. 3(d), obtained by the usual Fourier transform of the structure factor $S_X(Q)$, Fig. 3(b),

$$T_X(r) = 4\pi\rho_0 r + \frac{2}{\pi}\int_0^{Q_{max}} Q[S_X(Q) - 1]\sin QrM(Q)dQ, \quad (3)$$

where $M(Q)$ is a modification function and ρ_0 is the experimental number density, confirms characteristic differences between nanocrystalline and orthorhombic antimony sesquisulfides. The latter is formed by infinite quasi one-dimensional (1D) $(Sb_4S_6)_\infty$ ribbons oriented parallel to the b axis, Fig. 3(c). The inner Sb(II) atoms have 5 sulfur neighbors forming a distorted square pyramid with Sb(II) species located 0.17 Å below the basal plan of the pyramid. The outer Sb(I) counterparts reside at the apex of trigonal SbS_3 units connected by two-fold sulfur at the ribbon periphery and three-fold sulfur toward Sb(II) and the ribbon interior. The average intra-ribbon antimony coordination appears to be $\langle N_{Sb-S}^{intra}\rangle = 4$ while their sulfur neighbors have $\langle N_{S-Sb}^{intra}\rangle = 2.67$. The Sb(II)–S nearest neighbor (NN) distances reveal a strong Peierls distortion, $r_{Sb(II)-S}^{5F} = 2.70 \pm 0.16$ Å, while the intra-ribbon contacts for trigonal Sb(I) are uniform, $r_{Sb(I)-S}^{3F} = 2.53 \pm 0.01$ Å. The 1D-$(Sb_4S_6)_\infty$ entities are held together by rather strong inter-ribbon forces forming puckered sheets within the (a,c) plane. The shortest Sb–S inter-ribbon distances, $3.167 \leq r_{Sb-S}^{inter} \leq 3.642$ Å, are smaller than the sum of the van der Waals radii, $r_S^{vdW} = 1.8$ Å and $r_{Sb}^{vdW} = 2.2$ Å,[80] but larger than the Sb–S intra-ribbon NN contacts, $2.455 \leq r_{Sb-S}^{intra} \leq 2.854$ Å. The intra- and inter-ribbon separations are well distinguished using the $T_{Sbs}(r)$ partials for both orthorhombic and nanocrystalline Sb_2S_3, Fig. 3(d and e). The main difference between the two forms resides in the inter-ribbon connectivity. On average, each antimony in orthorhombic Sb_2S_3 has three short Sb–S inter-ribbon contacts, $\langle N_{Sb-S}^{inter}\rangle = 3$, while the connectivity in nc-Sb_2S_3 is reduced, $\langle N_{Sb-S}^{inter}\rangle \approx 1.5$. In other words, the 1D-$(Sb_4S_6)_\infty$ ribbons are becoming more isolated in the nanocrystalline lattice.

3.3 Raman spectroscopy and DFT modeling

Typical Raman spectra of glassy Sb_2S_3 as a function of temperature are shown in Fig. 4(b). The temperatures between $293 \leq T \leq 423$ K correspond to the solid glass, Fig. 4(a). Above $T_g = 492$ K, the supercooled liquid rapidly crystallizes at 523 K, Fig. 4(c), just in the vicinity of the DSC crystallization onset. Cooling down the crystallized sample, one obtains a typical spectrum of orthorhombic Sb_2S_3, characterized by multiple Raman-active modes $\Gamma = 10A_g + 5B_{1g} + 10B_{2g} + 5B_{3g}$, expected
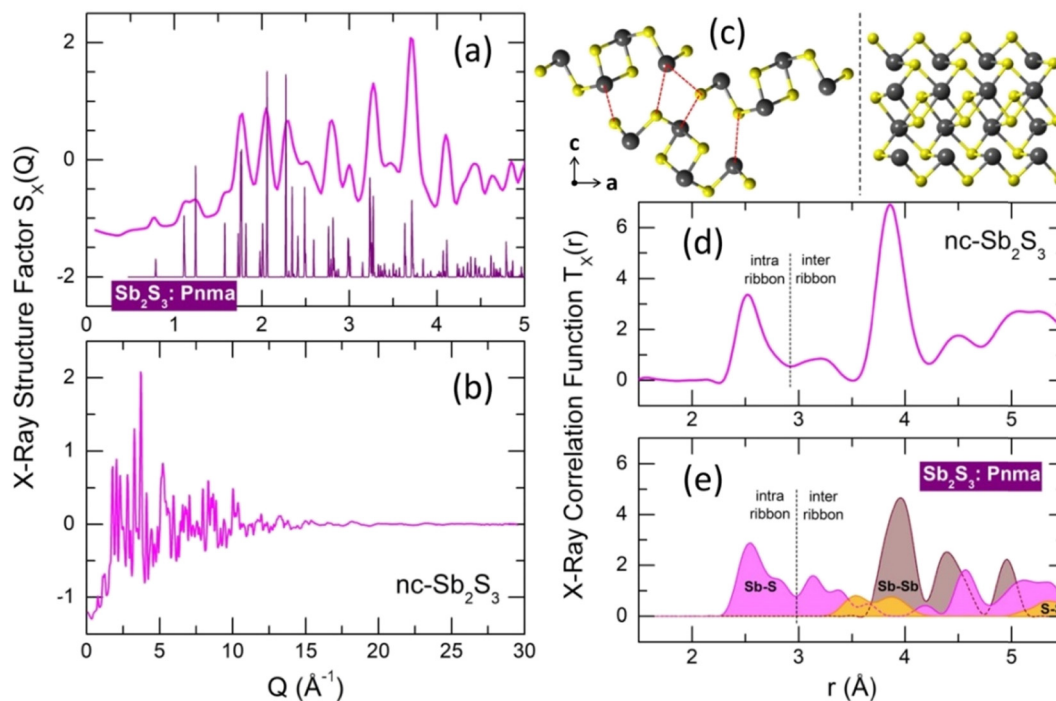
This journal is © The Royal Society of Chemistry 2023

J. Mater. Chem. C, 2023, **11**, 4654–4673 | **4657**

Fig. 3 Nanocrystalline (nc) and orthorhombic Sb_2S_3. (a) Bragg peaks of the nanocrystalline sample in comparison with the orthorhombic polymorph,[16] space group *Pnma*; (b) X-ray structure factor $S_X(Q)$ over the entire Q-range; (c) $(Sb_4S_6)_\infty$ ribbons in orthorhombic Sb_2S_3: left, atomic arrangements using projection on the (*a,c*) plane, right, a single ribbon oriented parallel to the *b* axis; (d) X-ray total correlation function $T_X(r)$ of nc-Sb_2S_3; (e) Sb–S (magenta), Sb–Sb (light brown) and S–S (yellow) $T_{ij}(r)$ partials for orthorhombic Sb_2S_3. The dashed red lines in (c), left panel, show the shortest inter-ribbon Sb–S distances (3.167–3.642 Å). The black dashed lines in (d and e) separate intra- (2.455–2.854 Å) and inter-ribbon Sb–S nearest contacts.

for the *Pnma* polymorph.[81] Usually, about ten modes are clearly distinguishable.[20,21,26]

The Raman spectrum of *L*-Sb_2S_3 at 873 K appears to be reminiscent of its glassy counterpart, Fig. 4(d), except for a strong S–S stretching at 490 cm^{-1}. Assuming a dissociation reaction $2Sb\text{–}S \rightleftarrows Sb\text{–}Sb + S\text{–}S$, we also should expect a broad Sb–Sb stretching at ≈ 145 cm^{-1} as in amorphous antimony,[82,83] also confirmed by DFT modeling (Fig. S2, ESI†). A low-frequency vibration feature below 180 cm^{-1} may contain both Sb–S bending and Sb–Sb stretching. We should however note that the appearance of intense S–S stretching in liquid Sb_2S_3 can be a transient phenomenon. Previously, both sulfur and antimony were detected on heating or laser-induced processing of amorphous Sb_2S_3 thin films, partly as intermediate species.[84–87] A limited accessible temperature range for our *in situ* Raman measurements does not enable further experiments at higher *T*. Nevertheless, temperature-dependent dynamics on melting was observed over a limited *T*-range, Fig. S3 (ESI†).

Basically, a broad asymmetric unresolved feature centered at $\nu_{max}^{Sb_2S_3} \approx 292$ cm^{-1} in glassy Sb_2S_3 is similar to that in *g*-As_2S_3 ($\nu_{max}^{As2S3} \approx 340$ cm^{-1}) but shifted to lower frequencies, Fig. 4(b), roughly scaling with the molecular mass ratio, $\nu_{max}^{Sb_2S_3}/\nu_{max}^{As_2S_3} \approx \sqrt{M_{As_2S_3}/M_{Sb_2S_3}}$. Amorphous *a*-$Sb_2S_3$ thin films and antimony-containing bulk sulfide glasses reveal similar vibrational features.[2,88–92] Assuming trigonal antimony local coordination[27] and the above resemblance in Raman spectra, various DFT

simulations have been carried out. Isolated pyramidal units SbS_3H_3, corner- $CS\text{-}Sb_2S_5H_4$ and edge-sharing $ES\text{-}Sb_2S_4H_2$ dimers of different conformation, and small rings, $Sb_3S_6H_3$ or $Sb_6S_{12}H_6$, systematically reveal overestimated Sb–S stretching frequencies, centered at $320 \le \langle\nu_{max}^{Sb\text{–}S}\rangle 350 \le$ cm^{-1}, Fig. S4 (ESI†). Reasonable results yield complicated clusters $Sb_{12}S_{18}H_2$ and $Sb_{12}S_{16}$, originating from the modified ribbons in orthorhombic Sb_2S_3 but with exclusively trigonal antimony coordination, Fig. 5. Both symmetric and asymmetric stretching frequencies, as well as low-frequency bending and deformation modes below 190 cm^{-1} are well reproduced by these clusters. As expected, the Sb–Sb stretching in $Sb_{12}S_{16}$ is overlapping with the Sb–S bending and deformation making it impossible to distinguish these vibrations experimentally. In contrast, the S–S stretching at 490 cm^{-1} is clearly visible in Raman scattering, Fig. 4(b and d), and confirmed by DFT simulations, Fig. S4 (ESI†), cluster $Sb_2S_6H_4$. The geometry of DFT-optimized size-limited clusters is consistent with crystalline references and glassy Sb_2S_3, Fig. S5 and S6 (ESI†), specifically that of $Sb_{12}S_{18}H_2$ and $Sb_{12}S_{16}$.

Raman spectroscopy measurements show that the glass structure hardly evolves at $T \lesssim T_g$; a negligible red shift of the Sb–S stretching envelope can only be observed, Fig. 4(b). The rapid crystallization above T_g seems to be related to the presence of modified structural motifs originating from the $(Sb_4S_6)_\infty$ entities, although the Sb(II) species lose their 5-fold coordination in the glass. Further insight into the atomic glass
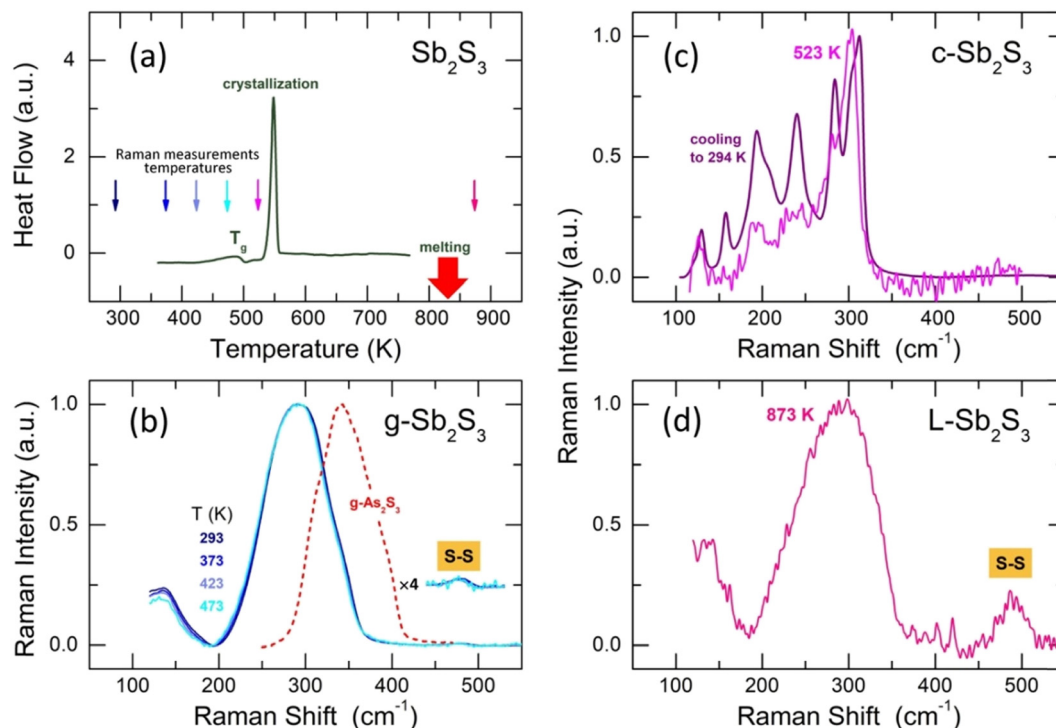
4658 | *J. Mater. Chem. C*, 2023, **11**, 4654–4673

This journal is © The Royal Society of Chemistry 2023

Fig. 4 Raman spectra of antimony sesquisulfide: (a) DSC trace of g-Sb$_2$S$_3$, the arrows show the Raman measurement temperatures; (b) spectra of a solid glass as a function of temperature, the insert shows S−S stretching at ≈490 cm^{-1}; (c) spectra of the orthorhombic polymorph at 523 K and after cooling to room temperature; (d) Raman spectrum of molten Sb$_2$S$_3$ at 873 K. The dashed red line in (b) also shows the As−S stretching envelope in g-As2S3. See the text for further details.
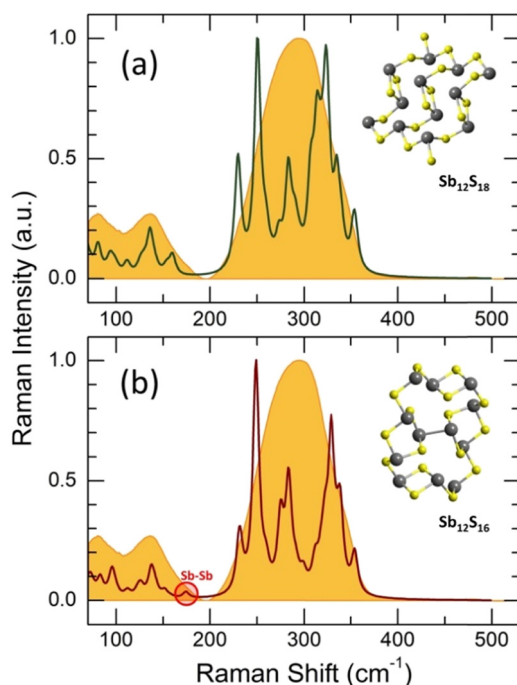

Fig. 5 DFT Raman spectra of (a) Sb$_{12}$S$_{18}$H$_2$ and (b) Sb$_{12}$S$_{16}$ size-limited clusters in comparison with the experimental Raman spectrum of g-Sb$_2$S$_3$, highlighted in yellow for the two panels. The terminal hydrogen species in (a) are omitted, and the H-related vibrations are removed from the spectrum. The inserts show DFT-optimized clusters. Weak Sb−Sb stretching in (b) is emphasized by the red circle.

structure yields high-energy X-ray diffraction supported by first-principles molecular dynamics (FPMD).

3.4 High-energy X-ray diffraction over the extended temperature range

Typical X-ray structure factors $S_X(Q)$ for g-Sb$_2$S$_3$, supercooled (673–773 K) and normal ($T \geq$ 843 K) liquids are shown in Fig. 6(a and b). The $S_X(Q)$s exhibit well-defined oscillations up to 30 Å^{-1}, ensuring high-resolution in the r-space. The oscillations amplitude decreases with increasing temperature but more significant changes are observed at low $Q \lesssim 5$ Å^{-1}.

Except for the distinct first sharp diffraction peak (FSDP) at $Q_0 = 1.22$ Å^{-1}, which is typical for a large majority of chalcogenide glasses (see, for example, Fig. S7 (ESI†) for glassy and liquid As$_2$S$_3$), vitreous Sb$_2$S$_3$ reveals an additional low-Q feature at $Q_{Sb} = 1.75$ Å^{-1}, specific for antimony, which emerges and increases in glassy (Sb$_2$S$_3$)$_x$(As$_2$S$_3$)$_{1-x}$ pseudo-binaries with increasing x.[71] Later, we will see that the 1.75 Å^{-1} feature corresponds to the principle peak PP$_{Sb}$ in the Sb−Sb partial structure factor $S_{SbSb}(Q)$, diverging from that in the $S_{SS}(Q)$ partial at $Q_S = 2.24$ Å^{-1} because of a large difference in atomic size of antimony and sulfur, whose covalent radii are r_{Sb} = 1.45 Å and $r_S = 1.03$ Å.[93,94] The FSDP and PP$_{Sb}$ are more visible after removing the background underneath the low-Q features using the subtraction procedure,[95,96] Fig. 6(c).

The FSDP amplitude $A_0(Q_0)$ slightly decreases in intensity with increasing T and shifts to lower Q, Fig. 6(c). In contrast,
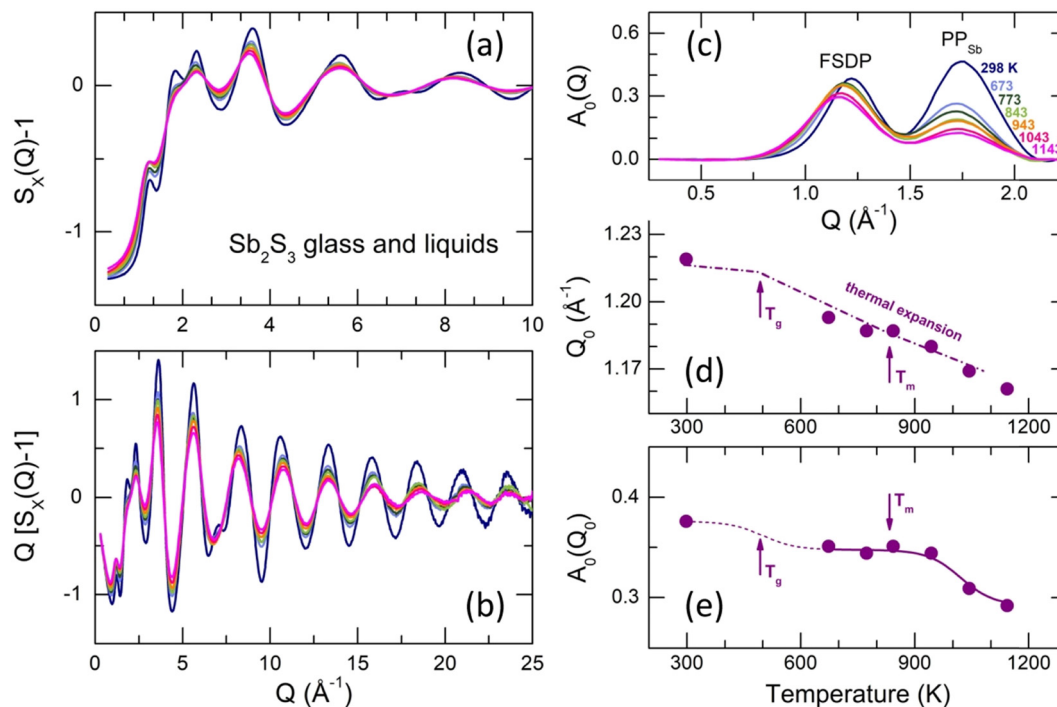
Fig. 6 High-energy X-ray diffraction data in Q-space for glassy and liquid Sb_2S_3: (a) X-ray structure factor $S_X(Q)$ over a limited Q-range and (b) interference function $Q[S_X(Q) - 1]$ as a function of temperature; (c) isolated first sharp diffraction peak (FSDP) and Sb–Sb diffraction feature PP_{Sb} as a function of temperature; (d) the FSDP position $Q_0(T)$ and (e) amplitude $A_0(Q_0, T)$. The dash-dotted line in (d) shows the expected $Q_0(T)$ trend taking into account the thermal expansion. The arrows show the glass transition temperature T_g and melting point T_m for Sb_2S_3. The solid and dashed lines in (e) are a guide to the eye.

changes in the PP_{Sb} amplitude are more significant (especially between the solid glass and liquids) and similar to other peaks and distant oscillations, Fig. 6(a and b). In addition, these temperature changes are characteristic for chalcogenide glasses and liquids, while the FSDP behaves differently. In particular, the FSDP position $Q_0(T)$ for Sb_2S_3 follows the thermal expansion, $Q_0(T) \propto \rho(T)^{1/3}$,[97] where $\rho(T)$ is the macroscopic number density.

The X-ray total correlation functions $T_X(r)$ for glassy and liquid Sb_2S_3, obtained by the usual Fourier transform of $S_X(Q)$, are shown in Fig. 7. The first peak at 2.484 ± 0.004 Å corresponds to Sb–S nearest neighbors followed by a strongly asymmetric second neighbor (2nd N) peak at 3.83 ± 0.02 Å with additional unresolved correlations between 2.8 and 3.4 Å. The third distinct feature at 5.7 Å seems to be related to a center-center distance between the Sb–S entities. All peaks become less intense and broader with increasing temperature, also leading to a stronger overlapping between NN and second neighbor correlations. More distant broad peaks at 7.3 and 9 Å appear to be hardly visible in L-Sb_2S_3. Gaussian fitting of the NN and 2nd N correlations is inappropriate because of the peak asymmetry. Typical fitting with asymmetric functions is shown in Fig. 7(a) and yields reasonable results. The average antimony coordination N_{Sb-X}, where X = S and/or Sb, was found to be trigonal and consisting of two contributions, $N_{Sb-X} = N_{Sb-S} + N_{Sb-Sb} = 2.90(5) + 0.10(5)$ (Fig. 7(c), and see also Table 1). The Sb–S and Sb–Sb NN distances slightly increase with

temperature; both interatomic separations, $r_{Sb-S} = 2.484 \pm 0.004$ Å and $r_{Sb-Sb} = 2.92 \pm 0.02$ Å, are consistent with crystalline and amorphous references for trigonal antimony sulfides and elemental Sb.[16–18,93,98] Typical broadening of the Sb–S NN feature as a function of temperature is shown in Fig. 7(f). Both supercooled and normal liquids Sb_2S_3 exhibit a monotonic increase of $w_{Sb-S}(T)$.

3.5 First-principles molecular dynamics modeling of glassy and liquid Sb_2S_3

The derived FPMD interference functions $Q[S_X(Q) - 1]$ and pair-distribution functions $g_X(r)$ for the two extremes in experimental series at 300 and 1150 K are shown in Fig. 8. As reported earlier,[56–59] the FPMD with hybrid functional PBE0 yields good agreement with experimental data for chalcogenide systems. The FPMD replicas in Q-space reproduce well both the positions and amplitudes of oscillations for $Q[S_X(Q) - 1]$, Fig. 8(a,b). As a result, the derived interatomic distances in r-space are also consistent with the diffraction results, Fig. 8(c,d). In contrast, FPMD modeling with the standard functional PBE suffers from over- or underestimated correlations in Q- and r-space as shown in Fig. S8 (ESI†).

The partial structure factors $S_{ij}(Q)$ and pair-distribution functions $g_{ij}(r)$ are revealed in Fig. 9(a and b). We note divergent positions of PP_{Sb} and PP_S for the $S_{SbSb}(Q)$ and $S_{SS}(Q)$ partials, as well as a negative amplitude of $S_{SbS}(Q)$ in this range, explaining the appearance of an additional low-Q feature at $Q_{Sb} = 1.75$ Å^{-1}

4660 | *J. Mater. Chem. C*, 2023, **11**, 4654–4673

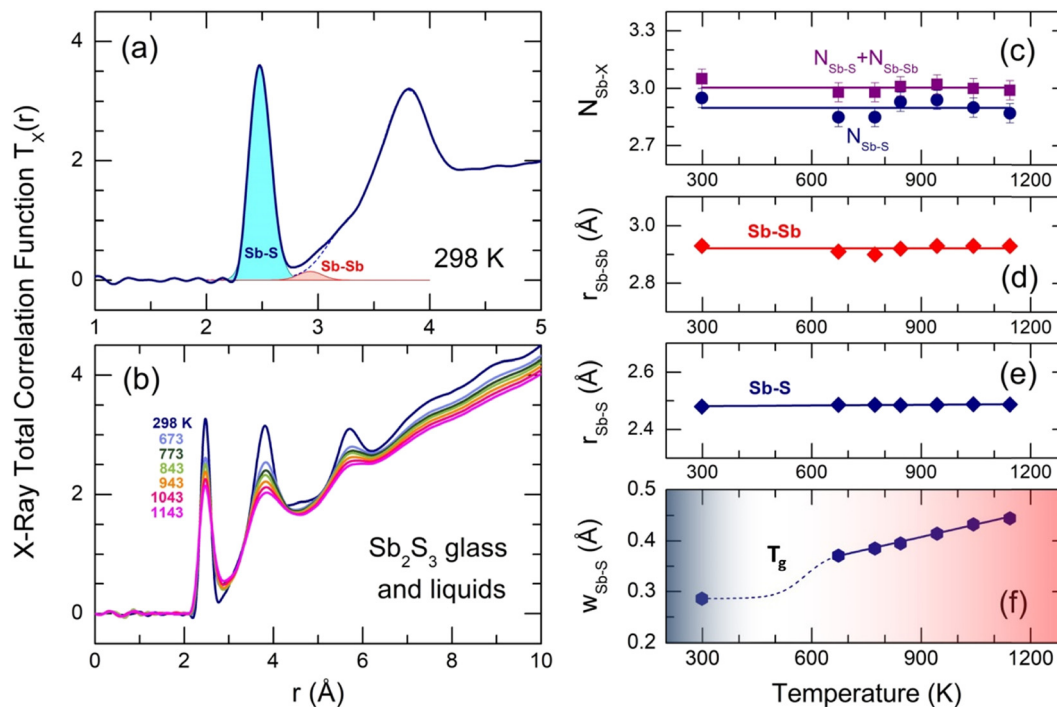This journal is © The Royal Society of Chemistry 2023

Fig. 7 High-energy X-ray diffraction data in r-space for glassy and liquid Sb_2S_3: (a) typical $T_X(r)$ fitting with asymmetric functions; Sb−S and Sb−Sb nearest neighbor (NN) correlations are highlighted in cyan and light red, respectively; (b) total correlation functions $T_X(r)$ over the temperature range 298 ≤ T ≤ 1143 K; (c) antimony local coordination number as a function of temperature; (purple squares) N_{Sb-S} + N_{Sb-Sb}, (dark blue circles) N_{Sb-S}; interatomic NN distances (d) Sb−Sb and (e) Sb−S as a function of T; (f) temperature dependence of asymmetric peak width for Sb−S NN correlations w_{Sb-S}; the solid glass and supercooled or normal liquid temperature domains are highlighted in blue and red, respectively. The dashed line in (f) is a guide to the eye. The other solid lines are a least-square fit of the experimental data.

Table 1 Interatomic distances r_{ij} and partial coordination numbers N_{ij} in glassy and liquid Sb_2S_3

Temperature (K)	S–S		Sb–S		Sb–Sb	
	r_{S-S} (Å)	N_{S-S}	r_{Sb-S} (Å)	N_{Sb-S}	r_{Sb-Sb} (Å)	N_{Sb-Sb}
High-energy X-ray diffraction						
298	—	—	2.480(6)	2.95(4)	2.93(2)	0.10(5)
673	—	—	2.486(6)	2.85(4)	2.91(2)	0.13(5)
773	—	—	2.486(6)	2.85(4)	2.90(2)	0.13(5)
843	—	—	2.485(6)	2.93(4)	2.92(2)	0.08(5)
943	—	—	2.486(6)	2.94(4)	2.93(2)	0.08(5)
1043	—	—	2.488(6)	2.90(4)	2.93(2)	0.10(5)
1143	—	—	2.487(6)	2.87(4)	2.93(2)	0.12(5)
First-principles molecular dynamics						
300	2.07	0.07	2.471	2.93	2.90	0.10
700	2.07	0.08	2.474	2.88	2.90	0.12
800	2.07	0.08	2.478	2.89	2.90	0.12
850	2.07	0.08	2.478	2.92	2.91	0.12
950	2.07	0.08	2.482	2.91	2.91	0.13
1050	2.08	0.08	2.480	2.95	2.90	0.13
1150	2.07	0.08	2.478	2.94	2.90	0.13

in the X-ray structure factor discussed above, Fig. 6(a–c). Astonishingly, the FSDP origin appears to be related to Sb–S correlations instead of the expected Sb–Sb counterparts. We note, however, that in glassy As_2S_3, the FSDP origin changes from As–As (major contribution) and As–S (minor component) at ambient pressure to mostly As–S correlations above 4 GPa, Fig. S9 (ESI†).

The partial pair-distributions $g_{ij}(r)$ are consistent with experimental findings. The Sb–S NN peak at 2.477 ± 0.004 Å exhibits an asymmetric shape, increasing with temperature, Fig. S10 (ESI†). The fitting with asymmetric functions yields very similar results to the experimental data, $\langle N_{Sb-S} \rangle$ = 2.91 ± 0.03, and the antimony local trigonal coordination is completed by the Sb–Sb nearest neighbors at 2.903 ± 0.002 Å, $\langle N_{Sb-Sb} \rangle$ = 0.12 ± 0.01, Table 1. The Sb–S second neighbors are located rather close to the Sb–S NN correlations and overlap significantly with increasing temperature despite the shift of r_{Sb-S}^{2nd} to higher distances from 3.36 Å (300 K) to 3.51 Å (1150 K), mostly because of a strong broadening of the NN and 2nd N correlations, Fig. S10 (ESI†).

The $g_{SS}(r)$ partial also shows S–S homopolar bonds at 2.07 Å, Fig. 9(b), $\langle N_{S-S} \rangle$ = 0.08 ± 0.01, Table 1. The Raman spectroscopy confirms this result, Fig. 4(b). Nevertheless, their concentration is too low to be observed by high-energy X-ray diffraction. In particular, Fig. 8(c and d) reveals that the S–S FPMD diffraction features are less intense compared to the experimental noise of $g_X(r)$.

Sulfur and antimony coordination distributions are plotted in Fig. 9(c and d). As expected, the overwhelming majority of the two species have a two-fold (91%) and trigonal (95%) local coordination, respectively. With increasing temperature, the population of two-fold sulfur and three-fold antimony decreases, while the fractions of under- and over-coordinated
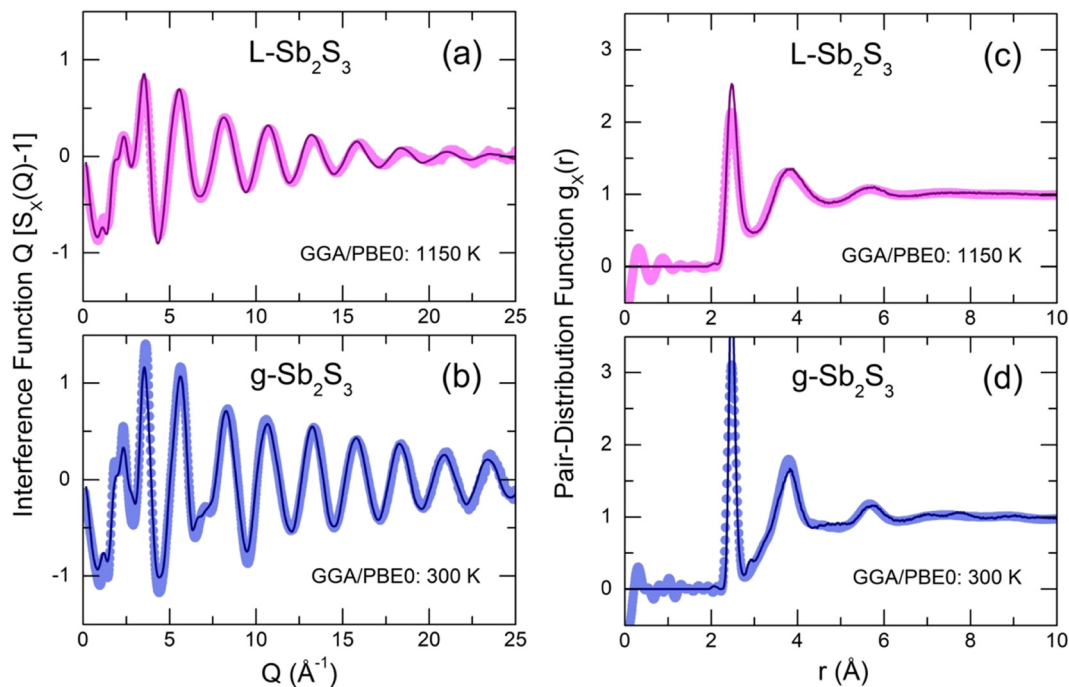
This journal is © The Royal Society of Chemistry 2023

J. Mater. Chem. C, 2023, 11, 4654–4673 | 4661

Fig. 8 FPMD modeling results using the hybrid functional GGA/PBE0 in comparison with experimental high-energy X-ray diffraction data for Sb_2S_3; interference function $Q[S_X(Q) - 1]$ at (a) 1150 K and (b) 300 K; pair-distribution function $g_X(r)$ at (c) 1150 K and (d) 300 K. The solid circles correspond to experimental data; the solid lines are the FPMD results.
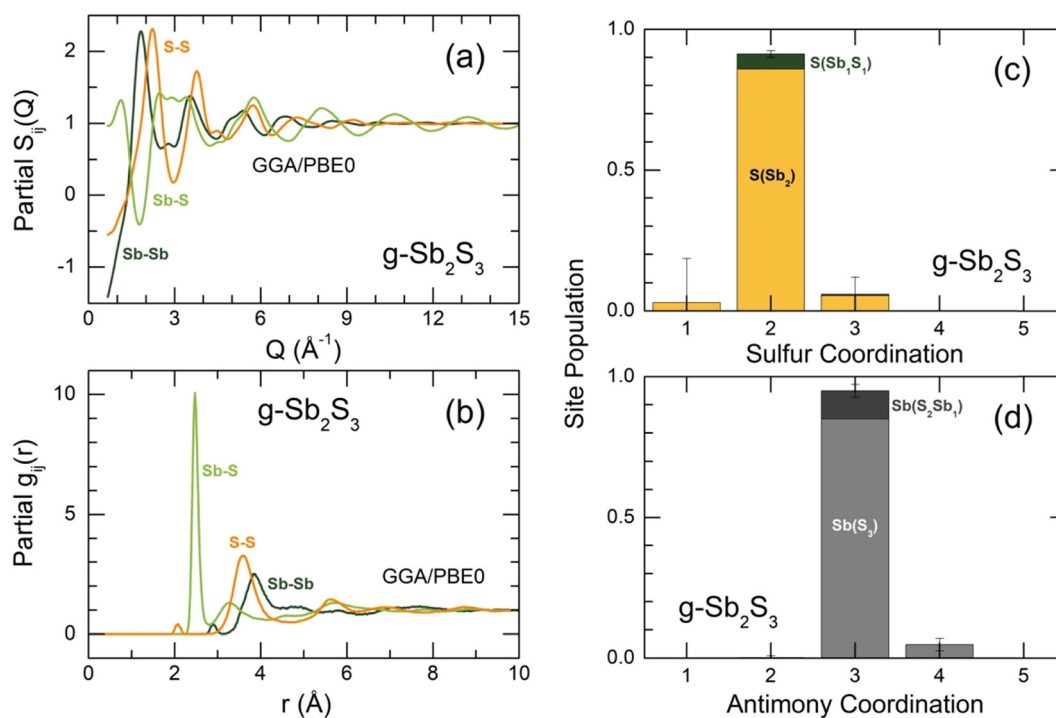

Fig. 9 Derived FPMD partial functions for glassy Sb_2S_3 at 300 K in (a) Q-space, $S_{ij}(Q)$, and (b) r-space, $g_{ij}(r)$; and local coordination numbers for (c) sulfur, N_{S-X}, and (d) antimony, N_{Sb-X}, where X = S or Sb.

species grow, Fig. S11 (ESI†). The number of sulfur or antimony local configurations with homopolar bonds, that is, $S(Sb_1S_1)$ instead of $S(Sb_2)$ or $Sb(S_2Sb_1)$ vs. $Sb(S_3)$ remains low at all temperatures.

4662 | J. Mater. Chem. C, 2023, 11, 4654–4673

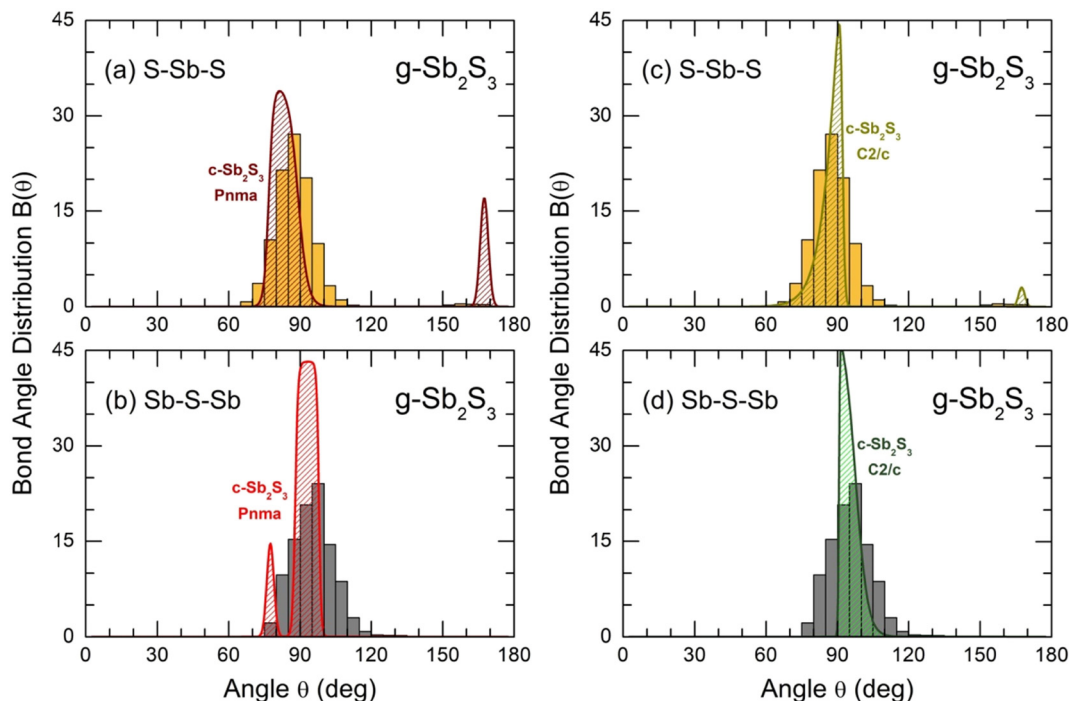This journal is © The Royal Society of Chemistry 2023

Fig. 10 Bond angle distributions $B(\theta)$ for glassy Sb_2S_3: (a) S–Sb–S and (b) Sb–S–Sb angles in comparison with orthorhombic Sb_2S_3, space group *Pnma*;[16] and (c) S–Sb–S and (d) Sb–S–Sb in comparison with monoclinic Sb_2S_3, space group *C2/c*.[18]

The bond angle distributions $B(\theta)$ for S–Sb–S and Sb–S–Sb triplets in glassy Sb_2S_3 are plotted in Fig. 10 in comparison with two crystalline counterparts: orthorhombic and monoclinic Sb_2S_3. The geometry of SbS_3 trigonal pyramids is different from that in canonical g-As_2S_3; the maximum of a broad asymmetric distribution $B_{SSbS}(\theta)$ is located at 87° opposite to 98° in arsenic sesquisulfide,[99] ensuring a more compact local structure of g-Sb_2S_3. Roughly speaking, SbS_3 pyramids can be considered as distorted defect octahedral entities, whose three missing Sb–S bonds became excessively long, and the corresponding sulfur species were transformed into the second neighbors. The above-mentioned fitting of $T_{SbS}(r)$ partials, Fig. S10 (ESI†), is consistent with this hypothesis, revealing three 2nd N correlations at ≈ 3.4 Å. The remnants of octahedral geometry are also evidenced by a weak contribution at $\theta \approx 160°$. The $B_{SSbS}(\theta)$ distributions in orthorhombic and monoclinic polymorphs are rather similar to that in the glass, especially in the high-temperature $C2/c$ form, including a low-intensity component at $168 \pm 4°$ of four-fold coordinated Sb(5)/Sb(6) species.[18] The 5-fold coordinated Sb(II) atoms in orthorhombic Sb_2S_3 yield an intense contribution at $\theta \approx 171°$.[16]

The connectivity of trigonal pyramids, reflected by $B_{SbSSb}(\theta)$ peaked at 97°, also appeared to be in favor of a more compact structure of glassy Sb_2S_3 compared to canonical g-As_2S_3. The $B_{AsSAs}(\theta)$ distribution in the latter has a maximum at 105°.[99] Crystalline Sb_2S_3 counterparts exhibit similar connectivities to glassy antimony sesquisulfide, slightly less evident for the orthorhombic polymorph.

As expected, the supercooled and normal Sb_2S_3 liquids are characterized by even more distorted Sb–S polyhedra and

polyhedral connectivities. Both $B_{SSbS}(\theta)$ and $B_{SbSSb}(\theta)$ distributions become broader and less symmetric with increasing temperature, Fig. S12 (ESI†).

The connectivity analysis shows that 96% of Sb and S are forming a single connected fragment. The homopolar bonds in the glass network are mostly related to few Sb–Sb and S–S dimers. Typical structural fragments in g-Sb_2S_3 are shown in Fig. 11(a). We note a certain similarity in the intermediate range order and ring statistics with orthorhombic and monoclinic polymorphs, Fig. 11, expected from the bond angle distributions. The orthorhombic crystal has ABAB squares (A: Sb; B: S) and six-membered rings Sb_3S_3; the monoclinic form, in addition to 6-fold entities, exhibits also big $Sb_{11}S_{11}$ rings, Fig. 11(g). Glassy and liquid Sb_2S_3 reveal a large variety of even- and odd-membered rings Sb_pS_q, $3 \leq p + q \leq 30$, related to chemical and topological disorder. Nevertheless, the most populated entities have size $p + q = 4$ and 6. The big rings, showing a broad distribution peaked at $p + q = 22$, become progressively unstable with increasing temperature. Their derived population $R_c(p + q)$[68] appears to be comparable with temporal fluctuations, reflected by the $R_c(p + q)$ uncertainty. At the highest temperature (1150 K), the population of ABAB squares exceeds any other $R_c(p + q)$, at least by a factor of 4, Fig. 11(b).

The ring statistics in g-As_2S_3 is rather similar to that in glassy antimony sesquisulfide. As it was reported previously,[99] the 12-membered rings As_6S_6, the only rings in monoclinic orpiment[100] and triclinic anorpiment[101] As_2S_3 are absent in glassy arsenic sulfide, Fig. 11(h).

More dense packing of glassy antimony sesquisulfide, evidenced by bond angle distributions $B_{SSbS}(\theta)$ and $B_{SbSSb}(\theta)$,
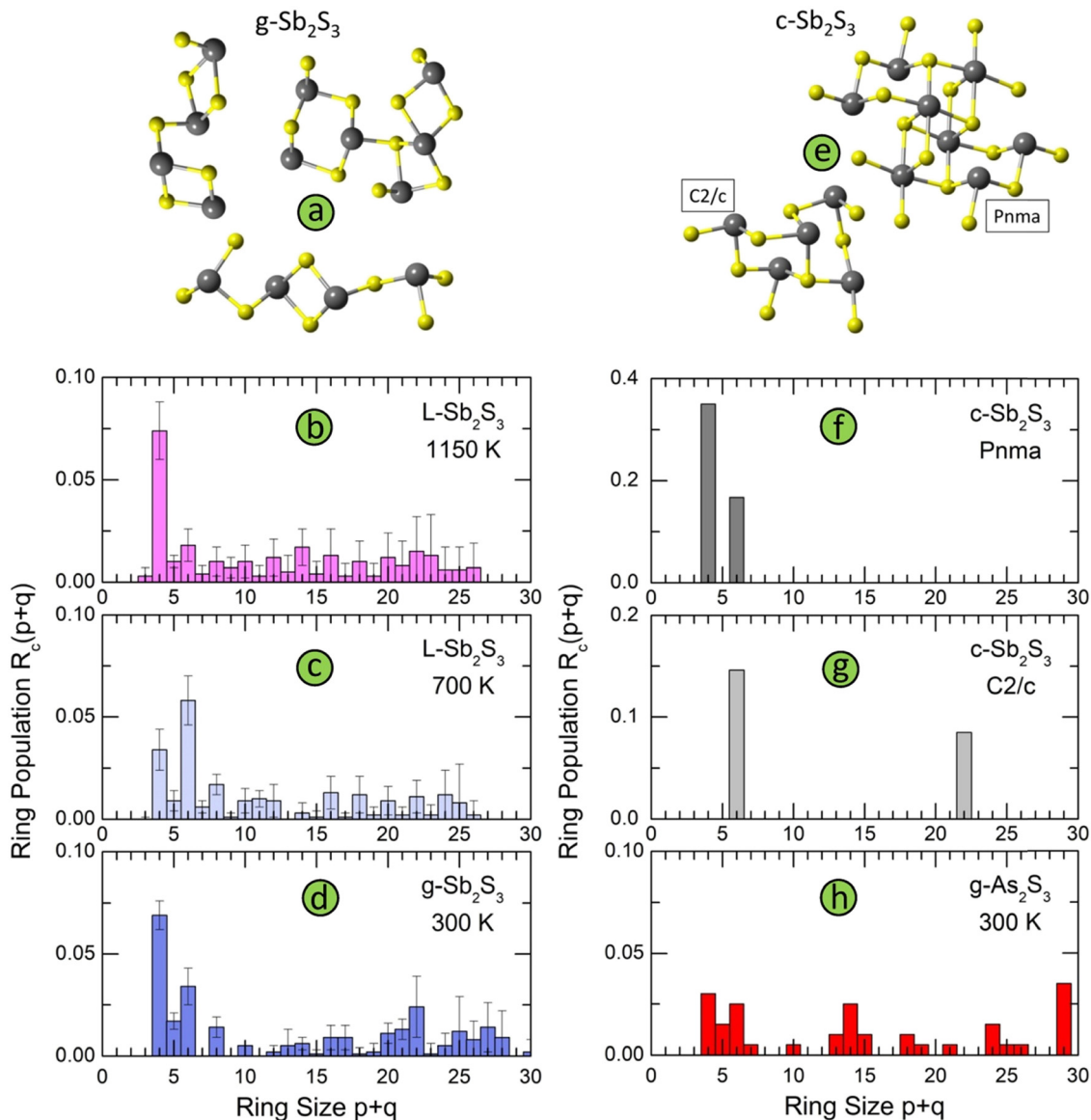
This journal is © The Royal Society of Chemistry 2023

J. Mater. Chem. C, 2023, **11**, 4654–4673 | **4663**

Fig. 11 Structural motifs and ring statistics; (a) typical fragments in g-Sb_2S_3; ring statistics in glassy, and liquid Sb_2S_3 as a function of temperature: (b) 1150 K (normal liquid), (c) 700 K (supercooled liquid), and (d) 300 K (solid glass); (e) structural motifs in monoclinic Sb_2S_3, space group $C2/c$,[18] and orthorhombic Sb_2S_3, space group $Pnma$;[16] ring statistics in (f) orthorhombic Sb_2S_3, (g) monoclinic Sb_2S_3, and (h) glassy As_2S_3.

suggests less microscopic voids and cavities in the glass network compared to g-As_2S_3. The Dirichlet–Voronoi tessellation[70] allows the cavity fraction V_c, normalized to the volume of the FPMD simulation box, $0 \leq V_c \leq 1$, to be computed. The results are given in Fig. 12 for the two sesquisulfides. As expected, the V_c in g-Sb_2S_3 is by a factor of two smaller than that of its arsenic counterpart, $21 \pm 1\%$ vs. $44 \pm 4\%$, respectively. The average size distribution of microscopic voids is rather similar in the two cases, $0.5 \leq r_c \leq 4$ Å, where r_c is the cavity radius, Fig. 12(a,b), although the average $\langle r_c \rangle$ is slightly smaller in glassy As_2S_3.

The partial pair-distribution functions $g_{AsS}(r)$ and $g_{SbS}(r)$ for g-As_2S_3/g-Sb_2S_3 yield additional evidence for a more compact or densified network in vitreous sulfides with increasing atomic number. Plotted on the normalized r/r_0 scale, where r_0 is the

As–S or Sb–S NN distance, the $g_{SbS}(r)$ shows a remarkable shift of the Sb–S second neighbors to shorter distances, approaching the NN shell, Fig. S13(a) in the ESI.† A similar more compact network compared to g-As_2S_3 under ambient conditions can be reproduced for glassy As_2S_3 under high pressure, e.g. in a diamond anvil cell at 6.3 GPa, Fig. S13(b), ESI.†

In summary, glassy and liquid antimony sesquisulfide has distinctly different structural features compared to orthorhombic Sb_2S_3. First, the antimony short range order in the crystal has a bimodal site distribution: 5-fold coordinated Sb(II) species with a strong Peierls distortion and regular trigonal Sb(I) entities. The Sb–S bonding asymmetry is absent in glassy and liquid polymorphs, characterized by a distorted antimony trigonal environment and shorter average $\langle r_{Sb-S}^{NN} \rangle$ distances,
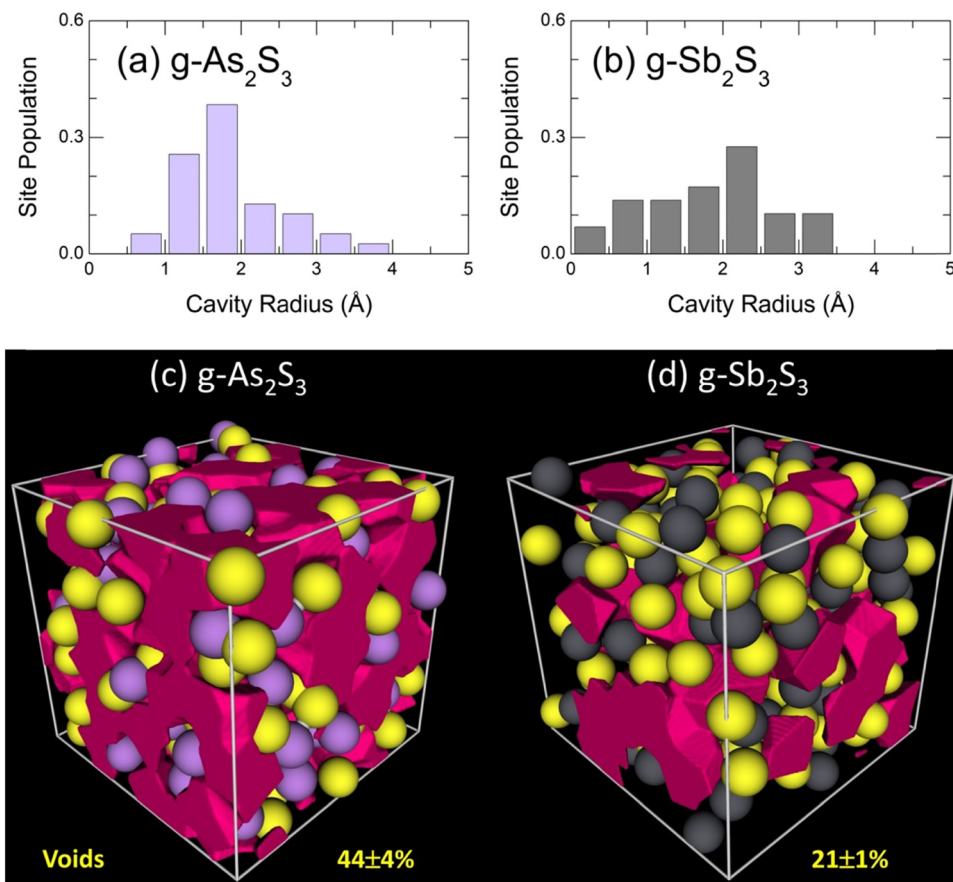
4664 | J. Mater. Chem. C, 2023, **11**, 4654–4673

This journal is © The Royal Society of Chemistry 2023

Fig. 12 Void statistics: characteristic cavity radii in glassy (a) As_2S_3 and (b) Sb_2S_3; microscopic voids in (c) g-As_2S_3 and (d) g-Sb_2S_3.

2.64 ± 0.15 Å (c-Sb_2S_3, *Pnma*) *vs.* 2.48 ± 0.01 Å (g- and L-Sb_2S_3). This difference is clearly seen by ^{121}Sb-Mössbauer spectroscopy,[102,103] which is very sensitive to the local antimony environment.

Second, the intermediate range order in orthorhombic and glassy Sb_2S_3 is also different. The crystal structure is composed of infinite 1D-$(Sb_4S_6)_\infty$ ribbons with rather strong inter-ribbon interactions, while the glass network has a 2D layered structure, roughly reminiscent of that in canonical As_2S_3 but with remarkable differences. We should note comparable glass transition temperatures for the two vitreous alloys, Fig. 1, similar shape of the Raman spectra, Fig. 4, identical pnictide and sulfur local coordination and resembling ring statistics. However, the topology of antimony defect octahedral sites SbS_3, evidenced by bond angle distributions, is closer to crystalline Sb_2S_3 forms than to vitreous As_2S_3.

3.6 Electronic structure and atomic dynamics in glassy and liquid Sb_2S_3

The total electronic density of states (eDOS), calculated from the Kohn–Sham eigenvalue spectra, is shown in Fig. 13. The valence band (VB) consists of three sub-bands between the Fermi energy E_F and -20 eV, as in a large majority of crystalline and glassy chalcogenides.[35,58,75,104–106] The upper asymmetric part, mostly involving sulfur and antimony p-electron populations,

shows a predominant contribution at -2.8 eV (g-Sb_2S_3 at 300 K) or -2.3 eV (L-Sb_2S_3 at 1050 K), related to S 3p lone pairs. The bonding states at lower energies consist of Sb 5p, 5d and 5s together with S 3p orbitals. The middle sub-band centered at -10.7 eV (g-Sb_2S_3) or -10.0 eV (L-Sb_2S_3) has predominantly the s-character as well as the low-energy part at approximately -15 eV. The bandgap for glassy ($E_g = 2.28$ eV) and liquid ($E_g = 1.06$ eV) antimony sesquisulfide are consistent with the reported optical data[1,76–79] and electrical measurements (Fig. 2).

The derived eDOS is in good agreement with experimental data[107] and previously reported simulation results.[22,106,108–110] We should however note that simulations with the standard functionals yield a strongly underestimated bandgap (roughly by a factor of 2) in addition to insufficient agreement with the nearest and second neighbor correlations (see also Fig. S8, ESI†).

The inverse participation ratio (IPR),[35,111] Fig. 13(a and d), characterizes the degree of localization of a single-particle Kohn–Sham eigenfunction $\psi(r)$

$$\text{IPR} = \frac{\int dr |\psi(r)|^4}{\left(\int dr |\psi(r)|^2\right)^2}. \qquad (4)$$

A small IPR value ($\propto N^{-1}$, where N is the number of atoms in the simulation box) corresponds to an extended (delocalized)
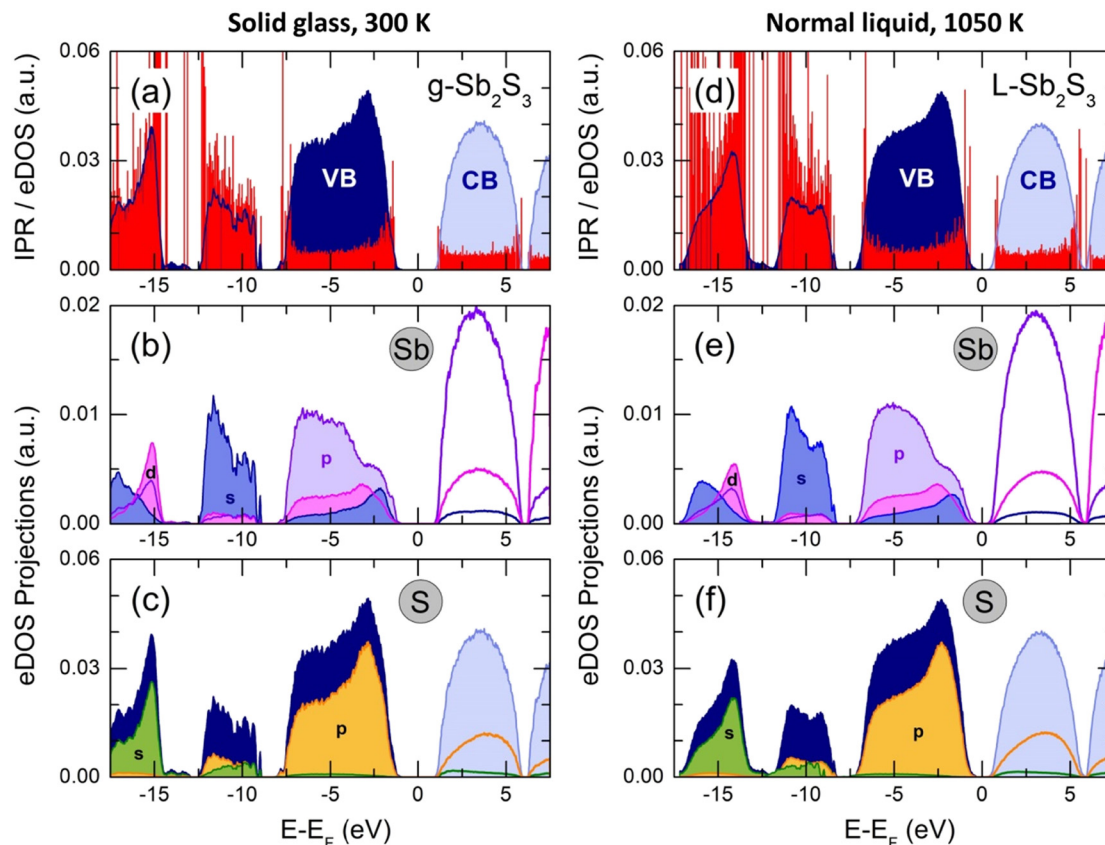
Fig. 13 Electronic properties of glassy and liquid Sb_2S_3; solid glass at 300 K: (a) the electronic density of states (eDOS) and the inverse participation ratio (IPR, red spikes), the projected eDOS (pDOS) on (b) antimony s (blue), p (violet), and d (magenta), and (c) sulfur s (green) and p (yellow) pseudo-wave functions; normal liquid at 1050 K: (d) eDOS and IPR, (e) antimony pDOS, and (f) sulfur pDOS. The valence band (VB) is highlighted in dark blue, the conduction band (CB) in light blue. See the text for further details.

wave function, while a large IPR (limIPR → 1) indicates a strong localization around a specific covalent bond. Similar to previously reported results[35,58,111] and theoretical predictions,[75] the electron states in glassy and liquid Sb_2S_3 are mostly localized at the band tails (that is, the top of the valence and the bottom of the conduction bands) and in lower-lying bonding states. The remaining electron states in the vicinity of the bandgap are delocalized.

Benchmark telluride PCMs are characterized by low viscosity and high fragility of the melt[112–116] ensuring fast atomic mobility at elevated temperature, which enables rapid crystallization within the nanosecond range, and a good retention of the amorphous phase in the vicinity of T_g and at lower T. The simulated dynamics in Sb_2S_3 reveals fast diffusion at high temperatures and a sudden decrease of diffusivity approaching the glass transition.

Typical Sb and S mean square displacements $\langle r^2(t) \rangle$ are shown in Fig. 14(a and b)

$$\langle r^2(t) \rangle = \left\langle \frac{1}{N_i} \left\{ \sum_{i=1}^{N_i} [r_i(t) - r_i(0)]^2 \right\} \right\rangle, \qquad (5)$$

where $r_i(0)$ and $r_i(t)$ are the positions of particle i for the initial time and time t, respectively, N_i is the total number of particles

i in the simulation box, and the angle brackets represent the average over the initial times. Below 30 fs, a ballistic regime is observed, mostly depending on temperature T and atomic mass m_i[117]

$$\langle r^2(t) \rangle \propto (k_B T / m_i) t^2, \qquad (6)$$

where k_B is the Boltzmann constant. On a log–log scale, the slope $s = 2$ is indicative of this regime, Fig. 14(b).

Above 5 ps, a diffusive motion is visible

$$\langle r^2(t) \rangle \propto D_i t, \qquad (7)$$

where D_i is the average diffusion coefficient of particles i, approaching the slope $s = 1$. The diffusion coefficients D_{Sb} and D_S were calculated using the Einstein equation

$$D_i = \frac{1}{6} \lim_{t \to \infty} \frac{\partial \langle r_i^2(t) \rangle}{\partial t}. \qquad (8)$$

The derived $D_{Sb}(T)$ and $D_S(T)$ are shown in Fig. S14 (ESI†), plotted on the Arrhenius scale and following thermally activated motion with temperature-dependent activation energy, $0.37 \leq E_d \leq 1.02$ eV in the vicinity of 1150 and 850 K, respectively.
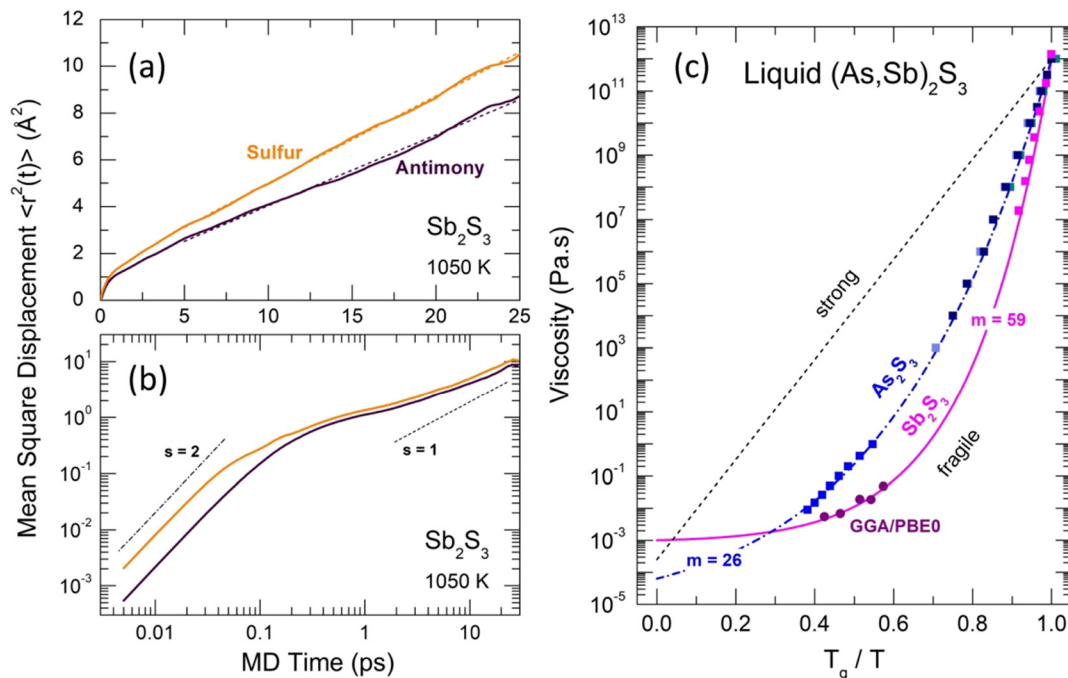
Paper

Fig. 14 Mean-square displacements $\langle r^2(t) \rangle$ and viscosity of Sb_2S_3. Antimony (dark purple) and sulfur (yellow) $\langle r^2(t) \rangle$ on (a) linear and (b) log–log scales. The dashed lines in (a) represent least-square fits of the $\langle r^2(t) \rangle$ data. The ballistic ($s = 2$) and diffusion ($s = 1$) regimes in (b) are shown by the dash-dotted and dashed lines, respectively. (c) Angell plot for the temperature dependence of viscosity $\eta(T)$ for As_2S_3 (blue) and Sb_2S_3 (magenta). The experimental viscosity data[118–123] are shown by the solid squares of different shades of blue for As_2S_3, and by the magenta squares for Sb_2S_3. The FPMD viscosity calculated using the Stokes–Einstein relation, eqn (9), is shown by the purple circles (this work). The dashed-dotted and solid lines represent the MYEGA[124] viscosity, eqn (10), for the two sesquisulfides. The derived fragility indices m are also shown. See the text for further details.

The Stokes–Einstein relationship was used to calculate the FPMD viscosity

$$\eta^{FPMD}(T) = \frac{k_B T}{6\pi D_{eff}(T) r_H}, \qquad (9)$$

where the effective atomic diffusion coefficient is $D_{eff}(T) = 0.4 D_{Sb}(T) + 0.6 D_S(T)$, and the effective temperature-dependent hydrodynamic radius r_H was determined using a Wigner–Seitz approach $r_{WS}(T) = \sqrt[3]{(3/4\pi) V_m(T) N_A^{-1}}$, where $V_m(T)$ is the melt molar volume and N_A is the Avogadro constant.

The derived viscosity is shown using an Angell plot, $\log \eta$ vs. T_g/T, Fig. 14(c), together with experimental viscosity data of different research groups for canonical As_2S_3 and Sb_2S_3.[118–123] The antimony sesquisulfide viscosity was obtained by extrapolation of the $(GeS_2)_x(Sb_2S_3)_{1-x}$ data, $0.1 \leq x \leq 0.9$.[123] At low $x \leq 0.5$, the $\log \eta(T,x)$ composition dependence is changing smoothly, enabling a reliable extrapolation of $\log \eta(T,x)$ to $x = 0$.

Both viscosities, $\eta(As_2S_3)$ and $\eta(Sb_2S_3)$, follow the Mauro–Yue–Ellison–Gupta–Allan (MYEGA) relationship[124] but with different fragilities

$$\log \eta(T) = \log \eta_0 + \left[\log \eta(T_g) - \log \eta_0 \right] \frac{T_g}{T}$$
$$\times \exp\left[\left(\frac{m}{\log \eta(T_g) - \log \eta_0} \right) \left(\frac{T_g}{T} - 1 \right) \right], \qquad (10)$$

where the fragility index $m = [\partial \log \eta / \partial (T_g/T)]_{T=T_g}$, η_0 and $\eta(T_g) = 10^{12}$ Pa s are the viscosity values at $T = \infty$ and T_g, respectively. The $m(As_2S_3) = 26$ is typical for canonical chalcogenide glasses with a network structure.[113–116,125,126] Antimony sesquisulfide exhibits a higher fragility, $m(Sb_2S_3) = 59$, approaching that of telluride PCMs.[113–116] We should also note good agreement between the experimental $\eta(T)$ and calculated $\eta^{FPMD}(T)$ viscosity.

We do not expect for Sb_2S_3 either a fragile-to-strong transition[112–115] or mesoscopic immiscibility accompanied by a viscosity anomaly[116,127] since both the experimental conductivity (Fig. 2) and FPMD simulations (Fig. 13) reveal a semiconducting behavior over the studied temperature range.

Nevertheless, we estimate that a semiconductor–metal (SC–M) transition is taking place between 1250 and 1550 K in comparison with $T_{SC–M} = 1600 \pm 150$ K for L-As_2S_3[114,128] (Fig. S15 and related details in the ESI†). We also note a lower SC-M transition temperature, 900 K $\lesssim T_{SC-M} \lesssim 1100$ K, for liquid antimony selenides.[114,129] In addition, anionic (Se) or cationic (Bi) substitution can be used for bandgap engineering, since E_g (Sb_2Se_3) = 1.0–1.3 eV[12,130] and E_g (Bi_2S_3) = 1.2–1.4 eV,[131,132] remaining within the wider gap materials compared to tellurides, E_g (Sb_2Te_3) = 0.5 eV.[133] Isomorphic mixed crystalline $Sb_2(S,Se)_3$ thin films were already studied for solar photovoltaics and exhibit the highest power conversion efficiency between Sb_2X_3-based tandem solar cells.[134,135] The anionic substitution is expected to be equally beneficial in smart

reprogrammable photonics for both SET and RESET logic states by tuning the bandgap within telecommunication wavelengths and improving the optical contrast, switching rate and energy efficiency. The cationic (Bi) doping is also started to be used in photovoltaics and seems to yield promising results.[136]

4. Concluding remarks

Summarizing the above observations, we can emphasize favorable features in the atomic structure and dynamics of vitreous and liquid Sb_2S_3 as a promising next-generation PCM for integrated smart photonics from the visible to telecom window. A high optical and electric contrast between the SET and RESET logic states in antimony sesquisulfide is based on a different short and intermediate range order in orthorhombic and amorphous Sb_2S_3. The orthorhombic polymorph is composed of quasi 1D-$(Sb_4S_6)_\infty$ ribbons with a strong asymmetry of the Sb–S nearest neighbor distances for three-fold and 5-fold antimony species ($2.46 \leq r_{Sb-S}^{NN} \leq 2.85$ Å) and significant inter-ribbon interactions. Glassy Sb_2S_3 reveals a 2D-disordered network built from defect octahedral entities SbS_3 ($r_{Sb-S}^{NN} = 2.48 \pm 0.01$ Å), whose three missing Sb–S bonds became excessively long, and the respective sulfur atoms were transformed into the second neighbors at ≈ 3.4 Å. A more compact network structure of g-Sb_2S_3 compared to canonical As_2S_3, evidenced by the bond angle distributions, shorter Sb–S second neighbor distances and a lower population of microscopic voids and cavities, appears to be a good compromise between the stability of the amorphous state and the ability of fast crystallization. An additional positive feature is related to the intermediate range structure of liquid Sb_2S_3, predominantly composed of ABAB squares, which are speeding up the crystallization phenomena. Another favorable aspect for the rapid SET-RESET transition is an enhanced fragility of liquid Sb_2S_3. The fragility index $m = 59$ is approaching those of the benchmark telluride PCMs and enables fast crystallization processes at elevated temperatures and simultaneously a remarkable slowdown in the vicinity of T_g, ensuring good retention of the amorphous phase. Furthermore, anionic (Se) and/or cationic (Bi) substitution may be used to decrease the temperature of a SC-M transition, thus improving the dynamics of the SET-RESET change, and allowing bandgap engineering equally important for photonics and photovoltaics.

Conflicts of interest

There are no conflicts to declare.

Acknowledgements

References

1 W. Dong, H. Liu, J. K. Behera, L. Lu, R. J. H. Ng, K. V. Sreekanth, X. Zhou, J. K. W. Yang and R. E. Simpson, Wide bandgap phase change material tuned visible photonics, *Adv. Funct. Mater.*, 2018, 1806181.

2 M. Delaney, I. Zeimpekis, D. Lawson, D. W. Hewak and O. L. Muskens, A new family of ultralow loss reversible phase-change materials for photonic integrated circuits: Sb_2S_3 and Sb_2Se_3, *Adv. Funct. Mater.*, 2020, 2002447.

3 H. Liu, W. Dong, H. Wang, L. Lu, Q. Ruan, Y. S. Tan, R. E. Simpson and J. K. W. Yang, Rewritable color nanoprints in antimony trisulfide films, *Sci. Adv.*, 2020, **6**, eabb7171.

4 S. Qin, N. Xu, H. Huang, K. Jie, H. Liu, J. Guo, H. Meng, F. Wang, X. Yang and Z. Wei, Near-infrared thermally modulated varifocal metalens based on the phase change material Sb_2S_3, *Opt. Express*, 2021, **29**, 7925–7934.

5 L. Lu, Z. Dong, F. Tijiptoharsono, R. J. H. Ng, H. Wang, S. D. Rezaei, Y. Wang, H. S. Leong, P. C. Lim, J. K. W. Yang and R. E. Simpson, Reversible tuning of Mie resonances in the visible spectrum, *ACS Nano*, 2021, **15**, 19722–19732.

6 W. Jia, R. Menon and B. Sensale-Rodriguez, Visible and near-infrared programmable multi-level diffractive lenses with phase change material Sb_2S_3, *Opt. Express*, 2022, **30**, 6808–6817.

7 L. Cao, X. Gao, B. Zhang, X. Ou, J. Zhang and W.-B. Luo, Bimetallic sulfide Sb_2S_3@FeS_2 hollow nanorods as high-performance anode materials for sodium-ion batteries, *ACS Nano*, 2020, **14**, 3610–3620.

8 S. Wang, Y. Cheng, H. Xue, W. Liu, Z. Yi, L. Chang and L. Wang, Multifunctional sulfur-mediated strategy enabling fast-charging Sb_2S_3 micro-package anode for lithium-ion storage, *J. Mater. Chem. A*, 2021, **9**, 7838–7847.

9 R. Chen, X. Lu, Q. He, M. Yao, T. Yao, A. Gao, S. Ding, Y. Cheng and H. Wang, Sb_2S_3 nanorod hierarchies enabling homogeneous sodium deposition for dendrite-free

4668 | *J. Mater. Chem. C*, 2023, **11**, 4654–4673

This journal is © The Royal Society of Chemistry 2023

sodium-metal batteries, *ACS Appl. Energy Mater.*, 2022, **5**, 10952–10960.

10 Y. Du, F. Liu, L. Jiang, M. Jia and Z. Zhang, Ultra-fine Sb_2S_3 particles encapsulated in activated-carbon: a high-performance anode for Li-ion batteries, *J. Alloys Compd.*, 2022, **907**, 164469.

11 W. Lian, C. Jiang, Y. Yin, R. Tang, G. Li, L. Zhang, B. Che and T. Chen, Revealing composition and structure dependent deep-level defect in antimony trisulfide photovoltaics, *Nat. Commun.*, 2021, **12**, 3260.

12 S. Barthwal, R. Kumar and S. Pathak, Present status and future perspective of antimony chalcogenide (Sb_2X_3) photovoltaics, *ACS Appl. Energy Mater.*, 2022, **5**, 6545–6585.

13 B. Roy, B. R. Chakraborty, R. Bhattacharya and A. K. Dutta, Electrical and magnetic properties of antimony sulphide (Sb_2S_3) crystals and the mechanism of carrier transport in it, *Solid State Commun.*, 1978, **25**, 937–940.

14 C. Chang, Y. Xiao, X. Zhang, Y. Pei, F. Li, S. Ma, B. Yuan, Y. Liu, S. Gong and L.-D. Zhao, High performance thermoelectrics from earth-abundant materials: enhanced figure of merit in PbS through nanostructuring grain size, *J. Alloys Compd.*, 2016, **664**, 411–416.

15 D. Bao, Q. Sun, L. Huang, J. Chen, J. Tang, D. Zhou, M. Hong, L. Yang and Z.-G. Chen, Thermoelectric performance of p-type (Bi,Sb)2Te3 incorporating amorphous Sb2S3 nanospheres, *Chem. Eng. J.*, 2022, **430**, 132738.

16 P. Bayliss and W. Nowacki, Refinement of the crystal structure of stibnite, Sb_2S_3, *Z. Kristallogr.*, 1972, **135**, 308–315.

17 D. O. McKee and J. T. McMullan, Comment on the structure of antimony trisulfide, *Z. Kristallogr.*, 1975, **142**, 447–449.

18 J. S. Swinnea, A. J. Tenorio and H. Steinfink, $Sb_{10}S_{15}$, a Pb-free analogue of fülöppite, $Pb_3Sb_8S_{15}$, *Am. Mineral.*, 1985, **70**, 1056–1058.

19 L. F. Lundegaard, R. Miletich, T. Balic-Zunic and E. Makovicky, Equation of state and crystal structure of Sb_2S_3 between 0 and 10 GPa, *Phys. Chem. Minerals*, 2003, **30**, 463–468.

20 J. Ibáñez, J. A. Sans, C. Popescu, J. López-Vidrier, J. J. Elvira-Betanzos, V. P. Cuenca-Gotor, O. Gomis, F. J. Manjón, P. Rodríguez-Hernández and A. Muñoz, Structural, vibrational, and electronic study of Sb_2S_3 at high pressure, *J. Phys. Chem. C*, 2016, **120**, 10547–10558.

21 I. Efthimiopoulos, C. Buchan and Y. Wang, Structural properties of Sb_2S_3 under pressure: evidence of an electronic topological transition, *Sci. Rep.*, 2016, **6**, 24246.

22 L. Dai, K. Liu, H. Li, L. Wu, H. Hu, Y. Zhuang, L. Yang, C. Pu and P. Liu, Pressure-induced irreversible metallization accompanying the phase transitions in Sb2S3, *Phys. Rev. B*, 2018, **97**, 024103.

23 Y. Wang, Y. Ma, G. Liu, J. Wang, Y. Li, Q. Li, J. Zhang, Y. Ma and G. Zou, Experimental observation of the high pressure induced substitutional solid solution and phase transformation in Sb_2S_3, *Sci. Rep.*, 2018, **8**, 14795.

24 Z. Cui, K. Bu, Y. Zhuang, M.-E. Donnelly, D. Zhang, P. Dalladay-Simpson, R. T. Howie, J. Zhang, X. Lü and Q. Hu, Phase transition mechanism and bandgap engineering of Sb_2S_3 at gigapascal pressures, *Commun. Chem.*, 2021, **4**, 125.

25 M. M. E. Ali, P. Kong, Y. Ni, H. Wang and Y. Chen, High pressure induced decomposition of antimony trisulfide, *Mater. Today Commun.*, 2021, **29**, 102828.

26 C. Hu, Y. Xu, Y. Gong, D. Yang, X. Li and Y. Li, Pressure-induced phase transitions, amorphization and alloying in Sb_2S_3, *Phys. Chem. Chem. Phys.*, 2022, **24**, 10053–10061.

27 L. Červinka and A. Hrubý, Structure of amorphous and glassy Sb_2S_3 and its connection with the structure of As_2X_3 arsenic – chalcogenide glasses, *J. Non-Cryst. Solids*, 1982, **48**, 231–264.

28 G. Dalba, P. Fornasini and G. Giunta, Short range order of amorphous Sb_2S_3 thin films: an X-ray diffraction study, *Solid State Commun.*, 1987, **62**, 773–776.

29 G. Dalba, P. Fornasini, G. Giunta and E. Burattini, XRD and EXAFS study of the local structure in some non-crystalline Sb-S compounds, *J. Non-Cryst. Solids*, 1989, **107**, 261–270.

30 M. Wuttig and N. Yamada, Phase-change materials for rewriteable data storage, *Nat. Mater.*, 2007, **6**, 824–832.

31 S. Raoux, W. Welnic and D. Ielmini, Phase change materials and their application to nonvolatile memories, *Chem. Rev.*, 2010, **110**, 240–267.

32 W. Zhang, R. Mazzarello, M. Wuttig and E. Ma, Designing crystallization in phase-change materials for universal memory and neuro-inspired computing, *Nat. Rev. Mater.*, 2019, **4**, 150–168.

33 B. J. Kooi and M. Wuttig, Chalcogenides by design: Functionality through metavalent bonding and confinement, *Adv. Mater.*, 2020, **32**, 1908302.

34 J. Akola, R. O. Jones, S. Kohara, S. Kimura, K. Kobayashi, M. Takata, T. Matsunaga, R. Kojima and N. Yamada, Experimentally constrained density-functional calculations of the amorphous structure of the prototypical phase-change material $Ge_2Sb_2Te_5$, *Phys. Rev. B: Condens. Matter Mater. Phys.*, 2009, **80**, 020201.

35 S. Caravati, M. Bernasconi and M. Parrinello, First-principles study of liquid and amorphous Sb_2Te_3, *Phys. Rev. B: Condens. Matter Mater. Phys.*, 2010, **81**, 014201.

36 A. V. Kolobov and J. Tominaga, *Chalcogenides: Metastability and Phase Change Phenomena*, Springer, Berlin, 2012, pp. 183–208.

37 S. Ahmed, X. Wang, H. Li, Y. Zhou, Y. Chen, L. Sun, W. Zhang and R. Mazzarello, Change in structure of amorphous Sb–Te phase-change materials as a function of stoichiometry, *Phys. Status Solidi RRL*, 2021, 2100064.

38 A. P. Hammersley, S. O. Svensson, M. Hanfland, A. N. Fitch and D. Häusermann, Two-dimensional detector software: from real detector to idealised image or two-theta scan, *High Pressure Res.*, 1996, **14**, 235–248.

39 L. B. Skinner, C. J. Benmore and J. B. Parise, Area detector corrections for high quality synchrotron X-ray structure factor measurements, *Nucl. Instrum. Methods Phys. Res.*, 2012, **662**, 61–70.

40 K. Ohara, Y. Onodera, S. Kohara, C. Koyama, A. Masuno, A. Mizuno, J. T. Okada, S. Tahara, Y. Watanabe, H. Oda, Y. Nakata, H. Tamaru, T. Ishikawa and O. Sakata, Accurate

This journal is © The Royal Society of Chemistry 2023

J. Mater. Chem. C, 2023, **11**, 4654–4673 | **4669**

synchrotron hard X-ray diffraction measurements on high-temperature liquid oxides, *Intern. J. Microgravity Sci. Appl.*, 2020, **37**, 370202.

41 S. Kohara, M. Itou, K. Suzuya, Y. Inamura, Y. Sakurai, Y. Ohishi and M. Takata, Structural studies of disordered materials using high-energy X-ray diffraction from ambient to extreme conditions, *J. Phys.: Condens. Matter*, 2007, **19**, 506101.

42 T. Usuki, M. Bokova, M. Kassem, K. Ohara, A. C. Hannon and E. Bychkov, Dimeric molecular structure of molten gallium trichloride and a hidden evolution toward a possible liquid–liquid transition, *J. Phys. Chem. B*, 2019, **123**, 10260–10266.

43 A. Tverjanovich, M. Khomenko, S. Bereznev, D. Fontanari, A. Sokolov, T. Usuki, K. Ohara, D. Le Coq, P. Masselin and E. Bychkov, Glassy GaS: transparent and unusually rigid thin films for visible to mid-IR memory applications, *Phys. Chem. Chem. Phys.*, 2020, **22**, 25560–25573.

44 M. J. Frisch, G. W. Trucks, H. B. Schlegel, G. E. Scuseria, M. A. Robb, J. R. Cheeseman, G. Scalmani, V. Barone, G. A. Petersson, H. Nakatsuji, X. Li, M. Caricato, A. V. Marenich, J. Bloino, B. G. Janesko, R. Gomperts, B. Mennucci, H. P. Hratchian, J. V. Ortiz, A. F. Izmaylov, J. L. Sonnenberg, D. Williams-Young, F. Ding, F. Lipparini, F. Egidi, J. Goings, B. Peng, A. Petrone, T. Henderson, D. Ranasinghe, V. G. Zakrzewski, J. Gao, N. Rega, G. Zheng, W. Liang, M. Hada, M. Ehara, K. Toyota, R. Fukuda, J. Hasegawa, M. Ishida, T. Nakajima, Y. Honda, O. Kitao, H. Nakai, T. Vreven, K. Throssell, J. A. Montgomery, Jr., J. E. Peralta, F. Ogliaro, M. J. Bearpark, J. J. Heyd, E. N. Brothers, K. N. Kudin, V. N. Staroverov, T. A. Keith, R. Kobayashi, J. Normand, K. Raghavachari, A. P. Rendell, J. C. Burant, S. S. Iyengar, J. Tomasi, M. Cossi, J. M. Millam, M. Klene, C. Adamo, R. Cammi, J. W. Ochterski, R. L. Martin, K. Morokuma, O. Farkas, J. B. Foresman and D. J. Fox, *Gaussian 16, revision C.01*, Gaussian, Inc., Wallingford, CT, 2016.

45 A. D. Becke, Density-functional thermochemistry. III. The role of exact exchange, *J. Chem. Phys.*, 1993, **98**, 5648–5653.

46 C. Lee, W. Yang and R. G. Parr, Development of the Colle-Salvetti correlation-energy formula into a functional of the electron density, *Phys. Rev. B: Condens. Matter Mater. Phys.*, 1988, **37**, 785–789.

47 D. Feller, The role of databases in support of computational chemistry calculations, *J. Comput. Chem.*, 1996, **17**, 1571–1586.

48 K. A. Peterson, D. Figgen, E. Goll, H. Stoll and M. Dolg, Systematically convergent basis sets with relativistic pseudopotentials. II. Small-core pseudopotentials and correlation consistent basis sets for the post-d group 16-18 elements, *J. Chem. Phys.*, 2003, **119**, 11113–11123.

49 G. B. Bacskay, A quadratically convergent Hartree-Fock (QCSCF) method. Application to closed shell systems, *Chem. Phys.*, 1981, **61**, 385–404.

50 P. Masselin, D. Le Coq, A. Cuisset and E. Bychkov, Spatially resolved Raman analysis of laser induced refractive index variation in chalcogenide glass, *Opt. Mater. Express*, 2012, **2**, 1768–1775.

51 A. Tverjanovich, A. Cuisset, D. Fontanari and E. Bychkov, Structure of Se-Te glasses by Raman spectroscopy and DFT modelling, *J. Am. Ceram. Soc.*, 2018, **101**, 5188–5197.

52 M. Kassem, M. Bokova, A. S. Tverjanovich, D. Fontanari, D. Le Coq, A. Sokolov, P. Masselin, S. Kohara, T. Usuki, A. C. Hannon, C. J. Benmore and E. Bychkov, Bent HgI_2 molecules in the melt and sulfide glasses: implications for nonlinear optics, *Chem. Mater.*, 2019, **31**, 4103–4112.

53 T. D. Kühne, M. Iannuzzi, M. Del Ben, V. V. Rybkin, P. Seewald, F. Stein, T. Laino, R. Z. Khaliullin, O. Schütt, F. Schiffmann, D. Golze, J. Wilhelm, S. Chulkov, M. H. Bani-Hashemian, V. Weber, U. Borštnik, M. Taillefumier, A. S. Jakobovits, A. Lazzaro, H. Pabst, T. Müller, R. Schade, M. Guidon, S. Andermatt, N. Holmberg, G. K. Schenter, A. Hehn, A. Bussy, F. Belleflamme, G. Tabacchi, A. Glöß, M. Lass, I. Bethune, C. J. Mundy, C. Plessl, M. Watkins, J. VandeVondele, M. Krack and J. Hutter, CP2K: An electronic structure and molecular dynamics software package – Quickstep: Efficient and accurate electronic structure calculations, *J. Chem. Phys.*, 2020, **152**, 194103.

54 J. P. Perdew, M. Ernzerhof and K. Burke, Rationale for mixing exact exchange with density functional approximations, *J. Chem. Phys.*, 1996, **105**, 9982–9985.

55 C. Adamo and V. Barone, Toward reliable density functional methods without adjustable parameters: the PBE0 model, *J. Chem. Phys.*, 1999, **110**, 6158–6170.

56 A. Tverjanovich, M. Khomenko, C. J. Benmore, M. Bokova, A. Sokolov, D. Fontanari, M. Kassem, T. Usuki and E. Bychkov, Bulk glassy $GeTe_2$: a missing member of the tetrahedral GeX_2 family and a precursor for the next generation of phase-change materials, *Chem. Mater.*, 2021, **33**, 1031–1045.

57 M. Bokova, A. Tverjanovich, C. J. Benmore, D. Fontanari, A. Sokolov, M. Khomenko, M. Kassem, I. Ozheredov and E. Bychkov, Unraveling the atomic structure of bulk binary Ga−Te glasses with surprising nanotectonic features for phase-change memory applications, *ACS Appl. Mater. Interfaces*, 2021, **13**, 37363–37379.

58 A. Tverjanovich, M. Khomenko, C. J. Benmore, S. Bereznev, A. Sokolov, D. Fontanari, A. Kiselev, A. Lotin and E. Bychkov, Atypical phase-change alloy Ga_2Te_3: atomic structure, incipient nanotectonic nuclei, and multilevel writing, *J. Mater. Chem. C*, 2021, **9**, 17019–17032.

59 M. Kassem, T. Bounazef, A. Sokolov, M. Bokova, D. Fontanari, A. C. Hannon, I. Alekseev and E. Bychkov, Deciphering fast ion transport in glasses: a case study of sodium and silver vitreous sulfides, *Inorg. Chem.*, 2022, **61**, 12870–12885.

60 S. Grimme, S. Ehrlich and L. Goerigk, Effect of the damping function in dispersion corrected density functional theory, *J. Comput. Chem.*, 2011, **32**, 1456–1465.

61 M. Micoulaut, Communication: van der Waals corrections for an improved structural description of telluride based materials, *J. Chem. Phys.*, 2013, **138**, 061103.

4670 | *J. Mater. Chem. C*, 2023, **11**, 4654–4673

This journal is © The Royal Society of Chemistry 2023

62 A. Bouzid, C. Massobrio, M. Boero, G. Ori, K. Sykina and E. Furet, Role of the van der Waals interactions and impact of the exchange-correlation functional in determining the structure of glassy GeTe₄, *Phys. Rev. B: Condens. Matter Mater. Phys.*, 2015, **92**, 134208.

63 T. Matsunaga, J. Akola, S. Kohara, T. Honma, K. Kobayashi, E. Ikenaga, R. O. Jones, N. Yamada, M. Takata and R. Kojima, From local structure to nanosecond recrystallization dynamics in AgInSbTe phase-change materials, *Nat. Mater.*, 2011, **10**, 129–134.

64 O. Gereben and L. Pusztai, RMC_POT, a computer code for Reverse Monte Carlo modeling the structure of disordered systems containing molecules of arbitrary complexity, *J. Comput. Chem.*, 2012, **33**, 2285–2291.

65 C. Hartwigsen, S. Goedecker and J. Hutter, Relativistic separable dual-space Gaussian pseudopotentials from H to Rn, *Phys. Rev. B: Condens. Matter Mater. Phys.*, 1998, **58**, 3641–3662.

66 S. Nosé, A molecular dynamics method for simulations in the canonical ensemble, *Mol. Phys.*, 1984, **52**, 255–268.

67 W. G. Hoover, Canonical dynamics: equilibrium phase-space distributions, *Phys. Rev. A*, 1985, **31**, 1695–1697.

68 S. Le Roux and P. Jund, Ring statistics analysis of topological networks: new approach and application to amorphous GeS₂ and SiO₂ systems, *Comput. Mater. Sci.*, 2010, **49**, 70–83.

69 S. Kohara, H. Ohno, M. Tabaka, T. Usuki, H. Morita, K. Suzuya, J. Akola and L. Pusztai, Lead silicate glasses: binary network-former glasses with large amounts of free volume, *Phys. Rev. B: Condens. Matter Mater. Phys.*, 2010, **82**, 134209.

70 I. Heimbach, F. Rhiem, F. Beule, D. Knodt, J. Heinen and R. O. Jones, pyMolDyn: identification, structure, and properties of cavities/vacancies in condensed matter and molecules, *J. Comput. Chem.*, 2017, **38**, 389–394.

71 Y. Kawamoto and S. Tsuchihashi, The properties and structure of glasses in the system As₂S₃-Sb₂S₃, *Yogyo-Kyokai-Shi*, 1969, **77**, 12–19.

72 K. N'Dri, J. Sei, D. Houphouet-Boigny, G. Kra and J.-C. Jumas, Estimation of glass-forming ability and glass stability of Sb₂S₃-As₂S₃-Sb₂Te₃ glasses by thermal properties, *J. Appl. Sci.*, 2007, **7**, 3167–3176.

73 K. N'Dri, D. Houphouet-Boigny, J.-C. Jumas and J. Olivier-Fourcade, Electronegativity difference, atomic size parameter and widths of supercooled liquid regions of Sb₂S₃-As₂S₃-Sb₂Te₃ glasses, *J. Non-Cryst. Solids*, 2011, **357**, 145–149.

74 G. J. Janz, F. W. Dampier, G. R. Lakshminarayanan, P. K. Lorenz and R. P. T. Tomkins, *Molten Salts: Volume 1, Electrical Conductance, Density, and Viscosity Data*, National Standard Reference Data Series; NBS 15, Washington D.C., 1968, p. 98.

75 N. F. Mott and E. A. Davis, *Electronic Processes in Non-Crystalline Materials*, 2nd edn, Clarendon Press, Oxford, 1979, pp. 28–37, 194–197, 491–497.

76 L. Guo, B. Zhang, S. Li, Q. Zhang, M. Buettner, L. Li, X. Qian and F. Yan, Scalable and efficient Sb₂S₃ thin-film solar cells fabricated by close space sublimation, *APL Mater.*, 2019, **7**, 041105.

77 J. Chen, J. Qi, R. Liu, X. Zhu, Z. Wan, Q. Zhao, S. Tao, C. Dong, G. Y. Ashebir, W. Chen, R. Peng, F. Zhang, S. Yang, X. Tian and M. Wang, Preferentially oriented large antimony trisulfide single-crystalline cuboids grown on polycrystalline titania film for solar cells, *Commun. Chem.*, 2019, **2**, 121.

78 C. Guo, J. Chen, G. Li, X. Liang, W. Lai, L. Yang, Y. Mai and Z. Li, Enhanced electrical conductivity of Sb₂S₃ thin film via C₆₀ modification and improvement in solar cell efficiency, *Global Challenges*, 2019, 1800108.

79 V. Lojpur, M. Joschko, C. Graf, N. Radmilović, M. Novaković and I. Validžić, Structural, morphological, optical, and electronic properties of amorphous non-Doped and I and Sn doped Sb₂S₃ nanoparticles, *Mater. Sci. Semicond. Processing*, 2022, **137**, 106196.

80 S. S. Batsanov, van der Waals radii of elements, *Inorg. Mater.*, 2001, **37**, 871–885.

81 Y. Liu, K. T. E. Chua, T. C. Sum and C. K. Gan, First-principles study of the lattice dynamics of Sb₂S₃, *Phys. Chem. Chem. Phys.*, 2014, **16**, 345–350.

82 J. S. Lannin, Raman scattering properties of amorphous As and Sb, *Phys. Rev. B: Solid State*, 1977, **15**, 3863–3871.

83 Z. Cheng, T. Milne, P. Salter, J. C. Kim, S. Humphrey, M. Booth and H. Bhaskaran, Antimony thin films demonstrate programmable optical nonlinearity, *Sci. Adv.*, 2021, **7**, eabd7097.

84 F. Perales, G. Lifante and F. Agulló-Rueda, and C. de las Heras, Optical and structural properties in the amorphous to polycrystalline transition in Sb2S3 thin films, *J. Phys. D: Appl. Phys.*, 2007, **40**, 2440–2444.

85 P. Makreski, G. Petruševski, S. Ugarković and G. Jovanovskic, Laser-induced transformation of stibnite (Sb₂S₃) and other structurally related salts, *Vib. Spectrosc.*, 2013, **68**, 177–182.

86 P. Parize, T. Cossuet, O. Chaix-Pluchery, H. Roussel, E. Appert and V. Consonni, In situ analysis of the crystallization process of Sb₂S₃ thin films by Raman scattering and X-ray diffraction, *Mater. Design*, 2017, **121**, 1–10.

87 J. Wang, Y. Qiao, T. Wang, H. Yu, Y. Feng and L. Li, Two-dimensional (2D) amorphous antimony (III) trisulfide nanosheets: synthesis, photoelectronic property and their transformation to crystalline 1D micro/nanorods, *Inorg. Chem. Comm.*, 2018, **92**, 110–114.

88 I. Watanabe, S. Noguchi and T. Shimizu, Study on local structure in amorphous Sb-S films by Raman scattering, *J. Non-Cryst. Solids*, 1983, **58**, 35–40.

89 Y. Gutiérrez, A. Fernández-Pérez, S. A. Rosales, C. Cobianu, M. Gheorghe, M. Modreanu, J. M. Saiz, F. Moreno and M. Losurdo, Polarimetry analysis and optical contrast of Sb₂S₃ phase change material, *Opt. Mater. Express*, 2022, **12**, 1531–1541.

90 J. Holubová, M. Liška, M. Chromčíková, E. Černošková and Z. Černošek, Structure of As₂S₃–Sb₂S₃ glasses by combined Raman spectroscopy and a thermodynamic modelling approach, *Phys. Chem. Glasses*, 2012, **53**, 31–36.

This journal is © The Royal Society of Chemistry 2023

J. Mater. Chem. C, 2023, **11**, 4654–4673 | **4671**

91 I. Pethes, V. Nazabal, J. Arib, I. Kaban, J. Darpentigny, E. Welter, O. Gutowski, B. Bureau, Y. Messaddeq and P. Jóvári, Atomic level structure of Ge-Sb-S glasses: chemical short range order and long Sb-S bonds, *J. Alloys Compd.*, 2019, **774**, 1009–1016.

92 S. Guan, S. Sun, D. Chen, J. Zhang, S. Kang, T. Xu and C. Lin, Formation and physical and structural properties of Sb_2S_3-PbI_2 chalcogenide glasses, *J. Non-Cryst. Solids*, 2021, **570**, 120993.

93 H. Krebs and R. Steffen, Neubestimmung der Nahordnung im glasigen Selen, im explosiven Antimon und im β- und γ-Arsen, *Z. Anorg. Allg. Chem.*, 1964, **327**, 224–237.

94 R. Winter, W.-C. Pilgrim, P. A. Egelstaff, P. Chieux, S. Anlauf and F. Hensel, Neutron scattering study on amorphous sulphur, *Europhys. Lett.*, 1990, **11**, 225–228.

95 E. Bychkov, C. J. Benmore and D. L. Price, Compositional changes of the first sharp diffraction peak in binary selenide glasses, *Phys. Rev. B: Condens. Matter Mater. Phys.*, 2005, **72**, 172107.

96 A. Bytchkov, G. J. Cuello, S. Kohara, C. J. Benmore, D. L. Price and E. Bychkov, Unraveling the atomic structure of Ge-rich sulfide glasses, *Phys. Chem. Chem. Phys.*, 2013, **15**, 8487–8494.

97 S. C. Moss and D. L. Price, Random packing of structural units and the first sharp diffraction peak in glasses, in *Physics of Disordered Materials*, ed. D. Adler, H. Fritzsche and S. Ovshinsky, Plenum, New York, 1985, pp. 77–95.

98 C. S. Barrett, P. Cucka and K. Haffner, The crystal structure of antimony at 4.2, 78 and 298° K, *Acta Cryst.*, 1963, **16**, 451–453.

99 S. I. Simdyankin, S. R. Elliott, Z. Hajnal, T. A. Niehaus and T. Frauenheim, Simulation of physical properties of the chalcogenide glass As_2S_3 using a density-functional-based tight-binding method, *Phys. Rev. B: Condens. Matter Mater. Phys.*, 2004, **69**, 144202.

100 D. J. E. Mullen and W. Nowacki, Refinement of the crystal structures of realgar, AsS and orpiment, As_2S_3, *Z. Kristallogr.*, 1972, **136**, 48–65.

101 A. R. Kampf, R. T. Downs, R. M. Housley, R. A. Jenkins and J. Hyrsl, Anorpiment, As_2S_3, the triclinic dimorph of orpiment, *Mineralog. Mag.*, 2011, **75**, 2857–2867.

102 E. Bychkov and G. Wortmann, ^{121}Sb-Mössbauer study of insulating and ion-conducting antimony chalcogenide-based glasses, *J. Non-Cryst. Solids*, 1993, **159**, 162–172.

103 M. A. El Idrissi Raghni, P. E. Lippens, J. Olivier-Fourcade and J. C. Jumas, Local structure of glasses in the As_2S_3-Sb_2S_3 system, *J. Non-Cryst. Solids*, 1995, **192–193**, 191–194.

104 F. Shimojo, K. Hoshino and Y. Zempo, Structural and electronic properties of liquid arsenic sulfide at high temperatures: ab initio molecular-dynamics simulations, *J. Phys. Soc. Japan*, 2005, **74**, 621–625.

105 J. Akola, P. Jóvári, I. Kaban, I. Voleská, J. Kolář, T. Wágner and R. O. Jones, Structure, electronic, and vibrational properties of amorphous AsS_2 and $AgAsS_2$: experimentally constrained density functional study, *Phys. Rev. B: Condens. Matter Mater. Phys.*, 2014, **89**, 064202.

106 X. Wang, Z. Li, S. R. Kavanagh, A. M. Ganose and A. Walsh, Lone pair driven anisotropy in antimony chalcogenide semiconductors, *Phys. Chem. Chem. Phys.*, 2022, **24**, 7195–7202.

107 J. Grigas, E. Talik and V. Lazauskas, X-ray photoelectron spectroscopy of Sb_2S_3 crystals, *Phase Transitions*, 2002, **75**, 323–337.

108 T. Ben Nasr, H. Maghraoui-Meherzi, H. Ben Abdallah and R. Bennaceur, Electronic structure and optical properties of Sb_2S_3 crystal, *Physica B*, 2011, **406**, 287–292.

109 M. Xu, R. Gu, C. Qiao, H. Tong, X. Cheng, C.-Z. Wang, K.-M. Ho, S. Wang, X. Miao and M. Xu, Unraveling the structural and bonding nature of antimony sesquichalcogenide glass for electronic and photonic applications, *J. Mater. Chem. C*, 2021, **9**, 8057–8065.

110 Y. Gutiérrez, A. P. Ovvyan, G. Santos, D. Juan, S. A. Rosales, J. Junquera, P. García-Fernández, S. Dicorato, M. M. Giangregorio, E. Dilonardo, P. Palumbo, M. Modreanu, J. Resl, O. Ishchenko, G. Garry, T. Jonuzi, M. Georghe, C. Cobianu, K. Hingerl, C. Cobet, F. Moreno, W. H. P. Pernice and M. Losurdo, Interlaboratory study on Sb2S3 interplay between structure, dielectric function, and amorphous-to-crystalline phase change for photonics, *iScience*, 2022, **25**, 104377.

111 J. Kalikka, J. Akola, R. O. Jones, S. Kohara and T. Usuki, Amorphous $Ge_{15}Te_{85}$: density functional, high-energy X-ray and neutron diffraction study, *J. Phys.: Condens. Matter*, 2012, **24**, 015802.

112 J. Orava, D. W. Hewak and A. L. Greer, Fragile-to-strong crossover in supercooled liquid Ag-In-Sb-Te studied by ultrafast calorimetry, *Adv. Funct. Mater.*, 2015, **25**, 4851–4858.

113 S. Wei, P. Lucas and C. A. Angell, Phase change alloy viscosities down to using Adam-Gibbs-equation fittings to excess entropy data: a fragile-to-strong transition, *J. Appl. Phys.*, 2015, **118**, 034903.

114 S. Wei, P. Lucas and C. A. Angell, Phase-change materials: the view from the liquid phase and the metallicity parameter, *MRC Bull.*, 2019, **44**, 691–698.

115 J. Pries, H. Weber, J. Benke-Jacob, I. Kaban, S. Wei, M. Wuttig and P. Lucas, Fragile-to-strong transition in phase-change material $Ge_3Sb_6Te_5$, *Adv. Func. Mater.*, 2022, 2202714.

116 W. Zhu, O. Gulbiten, B. Aitken and S. Sen, Viscosity, enthalpy relaxation and liquid-liquid transition of the eutectic liquid $Ge_{15}Te_{85}$, *J. Non-Cryst. Solids*, 2021, **554**, 120601.

117 R. Huang, I. Chavez, K. M. Taute, B. Lukić, S. Jeney, M. G. Raizen and E.-L. Florin, Direct observation of the full transition from ballistic to diffusive Brownian motion in a liquid, *Nat. Phys.*, 2011, **7**, 576–580.

118 A. P. Chernov, S. A. Dembovsky and V. M. Makhova, Viscosity and structure of glasses in the As2X3–AsI3 system, *Izv. Akad. Nauk SSSR, Neorg. Mater.*, 1970, **6**, 823–825.

119 N. E. Shchukina, G. M. Orlova and G. A. Chalabyan, The viscosity and elastic properties of glasses in the arsenic–sulfur–thallium system, *Fiz. Khim. Stekla*, 1979, **5**, 223–228.

4672 | *J. Mater. Chem. C*, 2023, **11**, 4654–4673

This journal is © The Royal Society of Chemistry 2023

120 S. V. Nemilov, The viscosity and elastic properties of melts and glasses in the As–S system and their valence-bond structure, *Fiz. Khim. Stekla*, 1979, **5**, 398–409.

121 G. Chaussemy, J. Fornazero and J.-M. Mackowski, Relationship between viscosity and structure in molten materials, *J. Non-Cryst. Solids*, 1983, **58**, 219–234.

122 A. S. Tverjanovich, Temperature dependence of the viscosity of chalcogenide glass-forming melts, *Glass Phys. Chem.*, 2003, **29**, 532–536.

123 J. Shánělová, P. Koštál and J. Málek, Viscosity of supercooled melts, *J. Non-Cryst. Solids*, 2006, **352**, 3952–3955.

124 J. C. Mauro, Y. Yue, A. J. Ellison, P. K. Gupta and D. C. Allan, Viscosity of glass-forming liquids, *Proc. Natl. Acad. Sci. U. S. A.*, 2009, **106**, 19780–19784.

125 P. Koštál, J. Shánělová and J. Málek, Viscosity of chalcogenide glass-formers, *Int. Mater. Rev.*, 2019, **65**, 63–101.

126 B. Yuan, B. G. Aitken and S. Sen, Viscoelastic behavior and fragility of Se-deficient chalcogenide liquids in As-P-Se system, *J. Non-Cryst. Solids X*, 2022, **16**, 100128.

127 M. Kassem, C. J. Benmore, T. Usuki, K. Ohara, A. Tverjanovich, M. Bokova, V. V. Brazhkin and E. Bychkov, Transient mesoscopic immiscibility, viscosity anomaly and high internal pressure at the semiconductor−metal transition in liquid Ga_2Te_3, *J. Phys. Chem. Lett.*, 2022, **13**, 10843–10850.

128 S. Hosokawa, Y. Sakaguchi, H. Hiasa and K. Tamura, Optical absorption spectra of liquid As_2S_3 and As_2Se_3 over a wide temperature range, *J. Phys.: Condens. Matter*, 1991, **3**, 6673–6677.

129 V. A. Alekseev, A. A. Andreev and M. V. Sadovskiĭ, Semiconductor-metal transition in liquid semiconductors, *Sov. Phys. Usp.*, 1980, **23**, 551–575.

130 X. Liang, Y. Feng, W. Dang, H. Huang, X. Wang, Y. Guo, K. Shen, R. E. I. Schropp, Z. Li and Y. Mai, High-efficiency flexible Sb_2Se_3 solar cells by back interface and absorber bulk deep-level trap engineering, *ACS Energy Lett.*, 2023, **8**, 213–221.

131 W. M. Linhart, S. J. Zelewski, P. Scharoch, F. Dybała and R. Kudrawiec, Nesting-like band gap in bismuth sulfide Bi_2S_3, *J. Mater. Chem. C*, 2021, **9**, 13733–13738.

132 M. Lan, Y. Wang, X. Dong, F. Yang, N. Zheng, Y. Wang, H. Ma and X. Zhang, Controllable fabrication of sulfur-vacancy-rich Bi_2S_3 nanorods with efficient near-infrared light photocatalytic for nitrogen fixation, *Appl. Surf. Sci.*, 2022, **591**, 153205.

133 J.-W. Park, S. H. Baek, T. D. Kang, H. Lee, Y.-S. Kang, T.-Y. Lee, D.-S. Suh, K. J. Kim, C. K. Kim, Y. H. Khang, J. L. F. Da Silva and S.-H. Wei, Optical properties of (GeTe, Sb_2Te_3) pseudobinary thin films studied with spectroscopic ellipsometry, *Appl. Phys. Lett.*, 2008, **93**, 021914.

134 Y. Zhao, S. Wang, C. Jiang, C. Li, P. Xiao, R. Tang, J. Gong, G. Chen, T. Chen, J. Li and X. Xiao, Regulating energy band alignment via alkaline metal fluoride assisted solution post-treatment enabling $Sb_2(S,Se)_3$ solar cells with 10.7% efficiency, *Adv. Energy Mater.*, 2022, **12**, 2103015.

135 S. Barthwal, R. Kumar and S. Pathak, Present status and future perspective of antimony chalcogenide (Sb_2X_3) Photovoltaics, *ACS Appl. Energy Mater.*, 2022, **5**, 6545–6585.

136 Y. Mao, L. Huang, W.-G. Zeng, F.-Y. Wu, L.-Q. Yao, L.-M. Lin, J.-M. Zhang, J.-M. Li and G.-L. Chen, Bi doping of Sb_2S_3 light-harvesting films: toward suitable energy level alignment and broad absorption for solar cells, *Chem. Eng. J.*, 2022, **446**, 137400.

This journal is © The Royal Society of Chemistry 2023

J. Mater. Chem. C, 2023, **11**, 4654–4673 | **4673**